Sloshing and slamming oscillations in a collapsible channel flow

PETER S. STEWART[1], MATTHIAS HEIL[2],
SARAH L. WATERS[3] AND OLIVER E. JENSEN[4]†

[1]Department of Engineering Sciences and Applied Mathematics, Northwestern University,
2145 Sheridan Road, Evanston, IL 60208, USA

[2]School of Mathematics, University of Manchester, Oxford Road, Manchester M13 9PL, UK

[3]Oxford Centre for Industrial and Applied Mathematics, University of Oxford,
24-29 St Giles', Oxford OX1 3LB, UK

[4]School of Mathematical Sciences, University of Nottingham, University Park,
Nottingham NG7 2RD, UK

We consider laminar high-Reynolds-number flow through a finite-length planar channel, where a portion of one wall is replaced by a thin massless elastic membrane that is held under longitudinal tension T and subject to a linear external pressure distribution. The flow is driven by a fixed pressure drop along the full length of the channel. We investigate the global stability of two-dimensional Poiseuille flow using a method of matched local eigenfunction expansions, which is compared to direct numerical simulations. We trace the neutral stability curve of the primary oscillatory instability of the system, illustrating a transition from high-frequency 'sloshing' oscillations at high T to vigorous 'slamming' motion at low T. Small-amplitude sloshing at high T can be captured using a low-order eigenmode truncation involving four surface-based modes in the compliant segment of the channel coupled to Womersley flow in the rigid segments. At lower tensions, we show that hydrodynamic modes increasingly contribute to the global instability, and we demonstrate a change in the mechanism of energy transfer from the mean flow, with viscous effects being destabilizing. Simulations of finite-amplitude oscillations at low T reveal a generic slamming motion, in which the flexible membrane is drawn close to the opposite rigid wall before recovering rapidly. A simple model is used to demonstrate how fluid inertia in the downstream rigid channel segment, coupled to membrane curvature downstream of the moving constriction, together control slamming dynamics.

Key words: flow–vessel interactions

1. Introduction

Throughout physiology there are numerous examples of flexible fluid-conducting vessels, such as blood flow in circulatory systems and gas and liquid flows in lung airways. Under certain conditions, the internal flow can be strongly coupled to deformation of the vessel, giving rise to nonlinear flow resistance properties (such as flow limitation in forced expiration) and instabilities manifested as Korotkoff noises
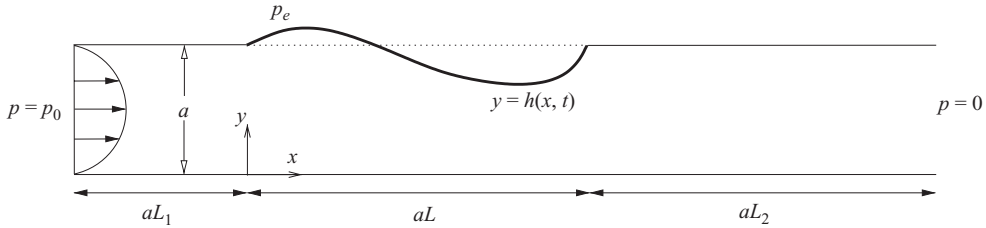
FIGURE 1. The two-dimensional analogue of a Starling resistor. Flow is driven by a fixed pressure drop p_0 through a channel, one wall of which contains a compliant massless membrane under external pressure p_e.

during sphygmomanometry and various respiratory sounds (wheezing from bronchial airways, snoring from the pharynx, vocalization from the larynx and birdsong from the syrinx) (see Grotberg & Jensen 2004; Thomson, Mongeau & Frankel 2005; Bertram 2008; Elemans *et al.* 2009; Dempsey *et al.* 2010). These applications raise some fundamental questions in fluid–structure interaction, such as: what are the mechanisms that drive instabilities; how, and to what extent, are instabilities in a compliant vessel coupled to distant regions of the flow domain; and what factors might regulate transient opposite-wall contact during an oscillation (e.g. during phonation)? The Starling resistor is a bench-top device, commonly used to investigate such questions, in which a flow is driven through a length of externally pressurized flexible tube that is mounted between two rigid pipes (Knowlton & Starling 1912). Vigorous self-excited oscillations are readily observed and have been mapped out in detail (Bertram, Raymond & Pedley 1990). However, despite the resistor's long history, many aspects of its dynamics remain poorly understood. We investigate these issues here through a theoretical study of a two-dimensional analogue of the Starling resistor (figure 1), a finite-length channel with a segment of one wall replaced by a massless tensioned membrane.

Early models of collapsible-tube flows have been reviewed elsewhere (Pedley & Luo 1998; Heil & Jensen 2003; Grotberg & Jensen 2004). Briefly, they may be classified either as studies of the full Starling resistor, accounting for the finite length of the system and the presence of rigid segments, or as studies of the local instabilities arising in spatially homogeneous flexible tubes or channels. Among the former category, models have progressed in sophistication from zero to three spatial dimensions. Low-dimensional models, which are relatively tractable (often at the expense of accuracy), have been successful in identifying basic physical mechanisms and in providing valuable overviews of parameter space. These have recently been complemented by more sophisticated two- and three-dimensional simulations that capture unsteady interactions between internal Navier–Stokes flows and a deforming elastic boundary (e.g. Luo & Pedley 1996; Luo *et al.* 2008; Heil & Boyle 2010).

Simulations of the flow in the two-dimensional Starling resistor analogue (figure 1), using boundary conditions of prescribed pressure or flux at either end of the channel, have revealed multiple modes of oscillation, which may be classified kinematically by the number of spatial extrema in the disturbance to the membrane location. Luo & Pedley (1996) showed how, when the membrane is subject to uniform external pressure (forcing it to adopt a non-uniform base state) and the upstream flux is prescribed, mode 2 oscillations can arise that are strongly coupled to a train of internal 'vorticity waves' downstream of the flexible segment; their role in the mechanism of instability is yet to be fully established. Luo *et al.* (2008) later showed the co-existence of modes

2–4 across distinct ranges of parameter space. Jensen & Heil (2003) demonstrated the existence of a mode 1 oscillation (with a single-humped membrane disturbance) that arises when the membrane is under high tension (and therefore has an approximately uniform base state); using an analytical model, they demonstrated that this high-frequency mode requires the upstream pressure (and not flux) to be prescribed and that the upstream rigid channel segment should be shorter than that downstream, a result confirmed in further simulations by Liu *et al.* (2009). While this kinematic modal classification of global modes is useful empirically, it may mask distinct physical mechanisms of instability, necessitating the use of approaches that probe the underlying dynamics.

   At present, only one mechanism of global instability in the two-dimensional Starling resistor analogue is well characterized in fundamental terms, namely the high-frequency mode 1 'sloshing' oscillation described using high-Reynolds-number asymptotics by Jensen & Heil (2003). This has also been captured using an approximate one-dimensional model of the same system by Stewart, Waters & Jensen (2009) and three-dimensional asymptotics and simulation for a non-axisymmetric tube by Heil & Waters (2008) and Whittaker *et al.* (2010*a*,*b*,*c*,*d*). Despite the increased complexity in higher dimensions, a common physical mechanism emerges. The channel (or tube) has an inviscid normal mode, in which transverse oscillations of the wall generate axial sloshing motions of the internal fluid; the frequency of oscillations is set by a balance between wall elasticity and fluid inertia. Provided the upstream supporting rigid segment is short, and the upstream pressure (rather than flux) is prescribed, sloshing is more vigorous at the upstream end of the system. In the presence of a mean flow, time-averaged sloshing motions can transport kinetic energy: if the sloshing is more vigorous upstream than downstream, it is possible for the normal mode to extract sufficient energy from the mean flow to overcome viscous losses arising through oscillations and adjustments to the mean flow. Asymptotic predictions of critical Reynolds numbers at which this global instability can grow have been validated against simulations capturing the full flow–structure interaction in both a two-dimensional flexible channel (Jensen & Heil 2003; see also figure 3*a*) and a three-dimensional elliptical tube (Whittaker *et al.* 2010*b*), in the limit in which the longitudinal tension is sufficiently large for the internal sloshing flow to have an inviscid core surrounded by thin Stokes layers. The relevance of this mechanism to instabilities arising at lower longitudinal tensions (and hence lower frequencies) is a question we address below.

   It is instructive to interpret the high-frequency global sloshing instability in terms of the underlying local modes of instability of the Poiseuille flow in homogeneous tubes or channels. These are either hydrodynamic modes, which may be perturbed by the presence of a flexible wall, or 'surface-based' or 'wall' modes, which exist only in flexible channels or tubes. Among the former group, we highlight two in particular: the Tollmien–Schlichting (TS) mode, which becomes unstable at sufficiently high Reynolds number (albeit much higher than values used in the simulations mentioned above) and which is a likely candidate for the vorticity waves observed by Luo & Pedley (1996); and, in a rigid channel, the 'Womersley' mode, corresponding to an axially uniform oscillatory flow, the two-dimensional analogue of the unsteady pipe flow described by Womersley (1955). For a channel having one wall rigid and the other a massless membrane, the wall modes are either 'static divergence' (SD) or 'travelling-wave flutter' (TWF) (following Carpenter & Garrad 1985, 1986): while SD is stable (in the absence of wall damping), TWF is long-wave unstable at all non-zero Reynolds numbers (Stewart, Waters & Jensen 2010*b*). Whereas TWF in a symmetric

flexible channel becomes unstable at high Reynolds numbers through the action of internal critical layers (Davies & Carpenter 1997) via a mechanism first identified by Miles (1957), in an asymmetric channel (as in figure 1), TWF is able to extract energy from the mean flow through viscous effects operating at an unusual 'weak' critical layer at the channel centreline (Stewart *et al.* 2010*b*), where the wave speed marginally exceeds the maximal speed of the parabolic base flow. We do not consider here additional flutter modes associated with membrane inertia.

High-frequency mode 1 sloshing in a two-dimensional channel was decomposed into its fundamental local components by Stewart *et al.* (2009), using a one-dimensional model. At small amplitudes, the global mode was shown to be a combination of Womersley modes in each rigid segment of the channel, coupled to a linear combination of the four wall modes in the compliant segment (i.e. upstream- and downstream-propagating SD and TWF). It was shown how the global mode can grow in time even when each local mode decays as it propagates up or down the compliant segment; global growth arises through wave reflections at the boundaries between the flexible and rigid segments. Because SD and TWF have simple asymptotic structures at high frequencies (an inviscid core flow with thin Stokes layers; Stewart *et al.* 2010*b*), the same modal combination was therefore captured (albeit implicitly) in the two-dimensional analysis of high-frequency sloshing by Jensen & Heil (2003). This remarkably simple representation of high-frequency sloshing (as a sum of four local wall-based eigenmodes in the compliant segment coupled to single Womersley modes in the rigid segments) has, in part, made it possible to capture this global mode asymptotically in three dimensions (Whittaker *et al.* 2010*b*).

The primary purpose of this paper is to extend this approach to determine how a wider class of global modes of the two-dimensional Starling resistor analogue (figure 1) might be represented in terms of expansions of underlying local eigenmodes. Having outlined the model (§2), in §3.1 we solve Orr–Sommerfeld problems to characterize the full spectra of local modes in both the rigid and compliant channel segments, without making any long-wavelength or high-frequency approximations. We then build truncated modal expansions in each segment, matching these across junctions using a formalism proposed by Manuilovich (2004); this is better suited to the present problem than the wave-driver approach of Sen *et al.* (2009). In addition to recovering small-amplitude, high-frequency sloshing, we use this approach in §4 to track the mode 1 neutral curve to relatively low Reynolds numbers (and low frequencies), demonstrating how hydrodynamic modes contribute increasingly to the global instability. This approach captures flow disturbances that propagate into the downstream rigid segment and reveals how locally generated instabilities (such as TWF) might contribute to global instability. We examine the energy budget of the neutrally stable modes (key balances are derived in §3.3) to identify the mechanism of energy transfer between the mean flow and the perturbation and to assess the accuracy of the modal expansions. The accuracy of the modal expansions is also tested in §4 against fully nonlinear two-dimensional numerical simulations of the coupled fluid and solid mechanics undertaken using the `oomph-lib` framework (§3.2, Heil & Hazel 2006) (`oomph-lib` is available as open-source software from http://www.oomph-lib.org), and against predictions of an existing one-dimensional model (Stewart *et al.* 2009). Additional simulations (presented in §5 and as an animation in the supplementary material, available at journals.cambridge.org/flm) reveal that, at lower Reynolds numbers, finite-amplitude mode 1 oscillations grow exponentially before saturating to a large-amplitude limit cycle, during which they exhibit vigorous but short-lived 'slamming'

motion, in which the membrane briefly comes into near contact with the opposite rigid wall. We present a reduced model to understand this near-singular behaviour, which again shows strong coupling between the flexible and rigid parts of the system.

2. The model

We consider a long rigid channel of width a and length L_0. A section of length aL of one wall of the channel is replaced by a thin elastic membrane subject to an external pressure p_e (figure 1). This membrane is held under longitudinal tension T_0. A Newtonian fluid, of density ρ and viscosity μ, is driven along the channel by a fixed pressure difference. We do not attempt to model in detail the manner in which pressure boundary conditions might be implemented experimentally; instead we either assume zero pressure at the downstream end of the channel and constant pressure p_0 at the upstream end, or else we implement equivalent traction boundary conditions in simulations (see §3.2).

As in Jensen & Heil (2003), we introduce a velocity scale $U_0 = p_0 a^2/(12\mu L_0)$ and non-dimensionalize by scaling all lengths on a, time on a/U_0 and pressure on ρU_0^2. The lengths of the upstream and downstream rigid sections of the channel are aL_1 and aL_2, respectively, so that $L_0 = a(L + L_1 + L_2)$. We define a Cartesian coordinate system, measuring x, the distance along the channel, from the intersection of the upstream rigid section and the flexible wall and y as the distance from the rigid wall. In $0 \leqslant x \leqslant L$, the compliant wall lies at $y = h(x, t)$, such that $h(0, t) = h(L, t) = 1$. We denote the fluid velocity field by $\boldsymbol{u} = (u, v)$ and the pressure by p. Incompressible fluid motion in the channel is governed by the two-dimensional Navier–Stokes equations (subscripts x, y and t denote derivatives; other subscripts do not):

$$u_x + v_y = 0, \tag{2.1a}$$

$$u_t + uu_x + vu_y = -p_x + R^{-1}(u_{xx} + u_{yy}), \tag{2.1b}$$

$$v_t + uv_x + vv_y = -p_y + R^{-1}(v_{xx} + v_{yy}). \tag{2.1c}$$

The model has five dimensionless parameters,

$$R = \frac{\rho a U_0}{\mu}, \quad T = \frac{T_0}{a\rho U_0^2}, \quad L, \quad L_1, \quad L_2, \tag{2.2}$$

where R is the Reynolds number and T the dimensionless longitudinal tension.

We denote the non-dimensional driving pressure at $x = -L_1$ by p_u, where

$$p_u = p_0/(\rho U_0^2) = 12(L + L_1 + L_2)/R. \tag{2.3}$$

The system admits steady, unit-flux Poiseuille flow along the channel when $h = 1$, which takes the form

$$\boldsymbol{u} = (U(y), 0) \equiv (6y(1-y), 0), \quad p = P(x) \equiv p_u - (12/R)(x + L_1). \tag{2.4}$$

We impose the non-uniform external pressure distribution

$$p_e(x) = P(x) \tag{2.5}$$

to ensure that there is no pressure difference across the flat membrane.

We apply no-slip and no-penetration conditions along the rigid portions of the channel. Across the membrane we apply no-slip and kinematic conditions:

$$u = 0, \quad v = h_t \quad (y = h). \tag{2.6}$$

The membrane is described using two essentially equivalent formulations. In computations (see §3.2), we employ geometrically nonlinear Kirchhoff–Love beam

theory (with the strain and bending tensors depending nonlinearly on the displacements) and assume incrementally linear elastic behaviour, characterized by an effective Young's modulus. The beam is assumed to have thickness $\mathfrak{h}$ and is subject to a (dimensional) pre-stress $T_0/\mathfrak{h}$. This formulation is exactly as given in Jensen & Heil (2003) and is implemented in the `oomph-lib` library (Heil & Hazel 2006). For ease of analysis, we also adopt a simpler approximation, which avoids the need to track Lagrangian wall elements and neglects bending and stretching effects. Provided $L \ll RT$, axial gradients in tension induced by viscous shear stresses are negligible; the shape of the membrane is then determined by a normal stress balance, which takes the form

$$p = p_e(x) - T h_{xx}, \tag{2.7}$$

assuming that membrane slopes are sufficiently small for the curvature to be linearized. The viscous component of the normal stress vanishes due to the boundary conditions (2.6).

The energy equation corresponding to (2.1) is

$$\tfrac{1}{2}(u^2 + v^2)_t + \tfrac{1}{2}(u(u^2 + v^2)_x + v(u^2 + v^2)_y)$$
$$= -(up)_x - (vp)_y + R^{-1}(u\nabla^2 u + v\nabla^2 v). \tag{2.8}$$

The corresponding energy budget, averaging across the channel and along each segment, can be written as a sum of five components in the form

$$\mathscr{K} + \mathscr{E} = \mathscr{P} + \mathscr{F} - \mathscr{D}, \tag{2.9a}$$

where

$$\mathscr{K}(t) = \frac{\mathrm{d}}{\mathrm{d}t}\left(\int_{-L_1}^{L+L_2} \int_0^h \frac{1}{2}(u^2 + v^2)\,\mathrm{d}y\,\mathrm{d}x\right), \tag{2.9b}$$

$$\mathscr{E}(t) = \int_0^L (vp)\Big|_{y=h}\,\mathrm{d}x, \tag{2.9c}$$

$$\mathscr{P}(t) = -\left[\int_0^1 up\,\mathrm{d}y\right]_{x=-L_1}^{x=L+L_2}, \tag{2.9d}$$

$$\mathscr{F}(t) = -\left[\int_0^1 \frac{1}{2}u(u^2 + v^2)\,\mathrm{d}y\right]_{x=-L_1}^{x=L+L_2}, \tag{2.9e}$$

$$\mathscr{D}(t) = -R^{-1}\int_{-L_1}^{L+L_2}\int_0^h (u\nabla^2 u + v\nabla^2 v)\,\mathrm{d}y\,\mathrm{d}x. \tag{2.9f}$$

Here, $\mathscr{K}$ is the net rate of change of kinetic energy, $\mathscr{E}$ is the rate of working of pressure forces across the membrane, $\mathscr{F}$ is the net kinetic energy flux, $\mathscr{P}$ is the rate of working of streamwise pressure forces and $\mathscr{D}$ is the rate of energy loss due to viscous dissipation. In the base state (2.4), $\mathscr{K} = \mathscr{E} = \mathscr{F} = 0$ and $\mathscr{P} = \mathscr{D} = -(12/R)(L + L_1 + L_2)$.

For later use we define the fluid vorticity as $\eta = v_x - u_y$. In addition, we denote the fluid flux along each segment of the channel by

$$q(x, t) = \int_0^h u\,\mathrm{d}y, \tag{2.10}$$

taking $h = 1$ in the rigid compartments. It is convenient to recall the one-dimensional approximation of the present system derived by Stewart *et al.* (2009). The governing

equations are simplified first by taking a long-wave approximation (assuming that $L \gg 1$, with L_1 and L_2 of comparable magnitude to L) and then by assuming a parabolic velocity profile $u = 6qy(h - y)/h^3$; this enables (2.1b) to be integrated in y to give coupled partial differential equations for the membrane location $h(x, t)$ and axial flux $q(x, t)$, which, in the present notation, are

$$h_t + q_x = 0, \tag{2.11a}$$

$$q_t + \frac{6}{5}\left(\frac{q^2}{h}\right)_x = Thh_{xxx} + \frac{12}{R}\left(h - \frac{q}{h^2}\right) \quad (0 \leqslant x \leqslant L). \tag{2.11b}$$

The same approach yields the following boundary conditions representing flows in the rigid upstream and downstream segments:

$$h = 1, \quad Th_{xx} = L_1[12R^{-1}(q - 1) + q_t] \quad (x = 0), \tag{2.11c}$$

$$h = 1, \quad Th_{xx} = -L_2[12R^{-1}(q - 1) + q_t] \quad (x = 1). \tag{2.11d}$$

The one-dimensional model (2.11) is tested against two-dimensional simulations below.

3. Methods

We study the stability of the uniform base state using two complementary approaches. In §3.1 we construct neutrally stable global modes of the linearized problem as a truncated expansion of the underlying local eigenmodes. In §4 these are compared to two-dimensional simulations of the full nonlinear problem treating the fluid and solid mechanics exactly, using a computational scheme outlined in §3.2. In §3.3 we present various representations of the energy budget, including one that provides a test of the accuracy of the modal expansions.

3.1. *Linear stability: modal analysis*

We perturb the base state (2.4) by expanding the variables in the form

$$(u, v, p, h) = (U(y), 0, P(x), 1) + \theta(u_1, v_1, p_1, h_1) + \theta^2(u_2, v_2, p_2, h_2) + \cdots, \tag{3.1}$$

where $\theta \ll 1$. Equations (2.1) at $O(\theta)$ reduce to

$$u_{1,x} + v_{1,y} = 0, \tag{3.2a}$$

$$u_{1,t} + Uu_{1,x} + U_y v_1 = -p_{1,x} + R^{-1}(u_{1,xx} + u_{1,yy}), \tag{3.2b}$$

$$v_{1,t} + Uv_{1,x} = -p_{1,y} + R^{-1}(v_{1,xx} + v_{1,yy}), \tag{3.2c}$$

subject to

$$u_1 = 0, \quad v_1 = 0 \quad (y = 0, -L_1 < x < L + L_2), \tag{3.2d}$$

$$u_1 = -U_y(1)h_1, \quad v_1 = h_{1,t} \quad (y = 1, 0 < x < L), \tag{3.2e}$$

$$u_1 = 0, \quad v_1 = 0 \quad (y = 1, -L_1 < x < 0, L < x < L + L_2). \tag{3.2f}$$

The normal stress balance across the membrane (2.7) takes the form

$$p_1 = -Th_{1,xx} \quad (y = 1, 0 < x < L). \tag{3.2g}$$

Given (3.2), the energy equation (2.8) in each compartment at $O(\theta)$ cancels trivially. The $O(\theta^2)$ energy budget is considered in §3.3.

We consider the vector of flow quantities $\boldsymbol{q}(x, y, t) = [u_1, v_1, p_1, \eta_1]^{\mathrm{T}}$, dropping the subscript 1 in the remainder of §3.1. We assume time dependence of the form

$$\boldsymbol{q}(x, y, t) = A\hat{\boldsymbol{q}}(x, y; \omega)\mathrm{e}^{-\mathrm{i}\omega t} + A^*\hat{\boldsymbol{q}}^*(x, y; \omega)\mathrm{e}^{\mathrm{i}\omega t}, \tag{3.3}$$

where ω is a real frequency (as appropriate for neutrally stable oscillations), A a complex amplitude and * a complex conjugate. We then express spatially growing or decaying modes as $\hat{q}(x, y; \omega) = \tilde{q}(y; k, \omega)\mathrm{e}^{\mathrm{i}kx}$, where k is a complex wavenumber. We first determine k as a function of ω in the rigid and compliant segments. Then, by matching eigenfunction expansions across the junctions at $x = 0$ and $x = L$, we seek conditions on R and T for global neutrally stable modes to exist.

3.1.1. *Local eigenmodes in the rigid segments*

We first consider the case $k \neq 0$. Dropping tildes, the stability problem (3.2a–d, f) in the rigid segments of the channel becomes

$$
\mathscr{L}q \equiv \mathscr{L}
\begin{bmatrix} u \\ v \\ p \\ \eta \end{bmatrix}
\equiv
\begin{bmatrix}
u_y - \mathrm{i}kv + \eta \\
v_y + \mathrm{i}ku \\
p_y - \mathrm{i}\omega v + \mathrm{i}kUv - \mathrm{i}k\eta R^{-1} \\
\eta_y + R(\mathrm{i}kp - \mathrm{i}\omega u + \mathrm{i}kUu + U_y v)
\end{bmatrix}
= \mathbf{0},
\tag{3.4a}
$$

subject to boundary conditions

$$
u(0) = u(1) = 0, \quad v(0) = v(1) = 0.
\tag{3.4b}
$$

For numerical purposes, (3.4) is expressed in terms of a streamfunction ϕ as

$$
u = \phi_y, \quad v = -\mathrm{i}k\phi,
\tag{3.5a}
$$

$$
p = (\mathrm{i}kR)^{-1}(\phi_{yyy} - k^2\phi_y) - (U - \omega/k)\phi_y - U_y\phi, \quad \eta = k^2\phi - \phi_{yy},
\tag{3.5b}
$$

which leads to the Orr–Sommerfeld equation (Schmid & Henningson 2001)

$$
(U - \omega/k)(\phi_{yy} - k^2\phi) - U_{yy}\phi - (\mathrm{i}kR)^{-1}(\phi_{yyyy} - 2k^2\phi_{yy} + k^4\phi) = 0 \quad (0 < y < 1),
\tag{3.6a}
$$

$$
\phi(0) = \phi(1) = 0, \quad \phi_y(0) = \phi_y(1) = 0.
\tag{3.6b}
$$

Following Manuilovich (2004), we define the inner product as

$$
\langle \boldsymbol{f}, \boldsymbol{g} \rangle = \sum_{j=1}^{4} \int_0^1 f_j g_j \, \mathrm{d}y.
\tag{3.7}
$$

The corresponding adjoint problem is

$$
\mathscr{L}^\dagger q^\dagger \equiv \mathscr{L}^\dagger
\begin{bmatrix} u^\dagger \\ v^\dagger \\ p^\dagger \\ \eta^\dagger \end{bmatrix}
\equiv
\begin{bmatrix}
-u_y^\dagger + \mathrm{i}kv^\dagger - \mathrm{i}\omega R\eta^\dagger + \mathrm{i}kRU\eta^\dagger \\
-v_y^\dagger - \mathrm{i}ku^\dagger + \mathrm{i}(k - \omega)p^\dagger + RU_y\eta^\dagger \\
-p_y^\dagger + \mathrm{i}kR\eta^\dagger \\
-\eta_y^\dagger + u^\dagger - \mathrm{i}kp^\dagger R^{-1}
\end{bmatrix}
= \mathbf{0},
\tag{3.8}
$$

subject to boundary conditions

$$
p^\dagger(0) = p^\dagger(1) = 0, \quad \eta^\dagger(0) = \eta^\dagger(1) = 0,
\tag{3.9}
$$

ensuring that $\langle \boldsymbol{q}^\dagger, \mathscr{L}\boldsymbol{q} \rangle = \langle \mathscr{L}^\dagger \boldsymbol{q}^\dagger, \boldsymbol{q} \rangle$. The adjoint solution can also be expressed using a streamfunction $\phi^\dagger$, where

$$
u^\dagger = \phi_{yy}^\dagger - k^2\phi^\dagger, \quad v^\dagger = (\mathrm{i}k)^{-1}(\phi_{yyy}^\dagger - k^2\phi_y^\dagger) - R(U - \omega/k)\phi_y^\dagger,
\tag{3.10a}
$$

$$
p^\dagger = \mathrm{i}kR\phi^\dagger, \quad \eta^\dagger = \phi_y^\dagger,
\tag{3.10b}
$$

which satisfies

$$(U - \omega/k)(\phi_{yy}^\dagger - k^2\phi^\dagger) + 2U_y\phi_y^\dagger - (ikR)^{-1}(\phi_{yyyy}^\dagger - 2k^2\phi_{yy}^\dagger + k^4\phi^\dagger) = 0 \quad (0 < y < 1), \tag{3.11a}$$

$$\phi^\dagger(0) = \phi^\dagger(1) = 0, \quad \phi_y^\dagger(0) = \phi_y^\dagger(1) = 0. \tag{3.11b}$$

We formulate the orthogonality properties of eigenmodes of $\mathscr{L}$ and $\mathscr{L}^\dagger$ by considering any two eigenfunctions $\boldsymbol{q}_m$ and $\boldsymbol{q}_n^\dagger$, which, respectively, satisfy (3.4) and (3.8) (with corresponding eigenvalues k_m and k_n), and the inner product

$$\langle \boldsymbol{q}_n^\dagger, \mathscr{L}\boldsymbol{q}_m \rangle - \langle \mathscr{L}^\dagger\boldsymbol{q}_n^\dagger, \boldsymbol{q}_m \rangle = 0, \tag{3.12}$$

which follows directly from the definition of the adjoint. Integration by parts leads to

$$(k_m - k_n) \int_0^1 (u_m v_n^\dagger + v_m(Up_n^\dagger - u_n^\dagger) - R^{-1}\eta_m p_n^\dagger + R(p_m\eta_n^\dagger + Uu_m\eta_n^\dagger)) \, dy = 0. \tag{3.13}$$

Thus, for disturbances of fixed frequency ω, the eigenvalues k of the regular system (3.4) and the adjoint system (3.8) must coincide (Schmid & Henningson 2001) and we have the orthogonality condition

$$\int_0^1 (u_m v_n^\dagger - v_m u_n^\dagger + Uv_m p_n^\dagger - R^{-1}\eta_m p_n^\dagger + R(p_m\eta_n^\dagger + Uu_m\eta_n^\dagger)) \, dy = C\delta_{nm}, \tag{3.14}$$

where C is an arbitrary constant which depends on n. Using notation similar to Manuilovich (2004), (3.14) can be written as

$$\langle \boldsymbol{q}_n^\dagger, \boldsymbol{H}\boldsymbol{q}_m \rangle = C\delta_{nm}, \tag{3.15}$$

where

$$\boldsymbol{H} = \begin{bmatrix} 0 & -1 & 0 & 0 \\ 1 & 0 & 0 & 0 \\ 0 & U & 0 & -R^{-1} \\ UR & 0 & R & 0 \end{bmatrix}. \tag{3.16}$$

We now turn to the case $k = 0$. As the rigid segments are of finite length, the system admits the planar analogue of the Womersley flow in a rigid tube (Womersley 1955). The linearized Navier–Stokes equations reduce to $-i\omega u = -p_x + R^{-1}u_{yy}$, $p_y = 0$, subject to $u(0) = u(1) = 0$, which can be solved to give

$$p(x) = \bar{A}(x + \bar{B}), \quad u(y) = -\omega^{-1}p_x Z(y), \quad v(y) = 0, \quad \eta(y) = i\omega^{-1}p_x Z_y(y), \tag{3.17a}$$

where $\bar{A}$ is a normalization constant, $\bar{B}$ is defined by the global boundary conditions, $m \equiv \exp(-i\pi/4)(R\omega)^{1/2}$ and

$$Z(y; m) \equiv \left(1 - \frac{\sinh(m(1-y)) + \sinh(my)}{\sinh(m)}\right). \tag{3.17b}$$

The corresponding adjoint under the inner product (3.7) takes the simple form

$$u^\dagger = 0, \quad v^\dagger = D, \quad p^\dagger = 0, \quad \eta^\dagger = 0, \tag{3.18}$$

where D is a normalization constant which can be chosen as unity without loss of generality.

For $n = 1, 2, \ldots$, the wavenumbers of the hydrodynamic modes at fixed frequency ω satisfying (3.4) and (3.6) are denoted by $k_{r,n}$ (r for rigid); we label the corresponding
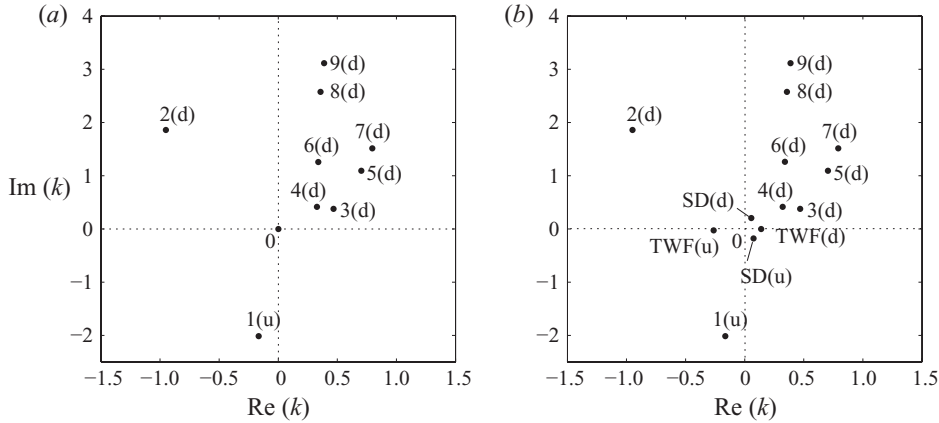
FIGURE 2. Local modes in the (*a*) rigid and (*b*) compliant segments of the channel, for $T = 100$, $R = 183.1$ and $\omega = 0.3557$. The terms (u) and (d), respectively, denote upstream- and downstream-propagating modes.

eigenfunctions with the subscript u (d) for the flow in the upstream (downstream) rigid segment. The eigenvalues and eigenfunctions are computed using a Chebyshev spectral method similar to that discussed by Stewart *et al.* (2010*b*) and summarized in Appendix A.1. The eigenvalue spectrum for a typical point in parameter space is illustrated in figure 2(*a*), with eigenvalues labelled as shown. Furthermore, '0' denotes the Womersley mode, '1' the least damped upstream-propagating mode and '2' the corresponding downstream-propagating mode with negative real part; remaining modes are ordered by increasing imaginary part. By continuation in R, we can identify mode '6' as the TS mode.

We then express the flow in the rigid compartments of the channel as modal expansions of the form

$$\boldsymbol{q}_u(x, y; \omega) = c_{u,0}\boldsymbol{q}_{u,0}(x, y) + \sum_{j=1}^{\infty} c_{u,j}\boldsymbol{q}_{u,j}(y)e^{ik_{r,j}x} \quad (-L_1 < x < 0), \qquad (3.19a)$$

$$\boldsymbol{q}_d(x, y; \omega) = c_{d,0}\boldsymbol{q}_{d,0}(x, y) + \sum_{j=1}^{\infty} c_{d,j}\boldsymbol{q}_{d,j}(y)e^{ik_{r,j}x} \quad (L < x < L + L_2), \quad (3.19b)$$

where $c_{u,j}$ and $c_{d,j}$ are unknown constants, which can be complex. Modes $\boldsymbol{q}_{u,0}$ and $\boldsymbol{q}_{d,0}$ correspond to (3.17).

3.1.2. *Local eigenmodes in the compliant segment*

In the compliant segment, the stability problem becomes (3.4*a*) subject to boundary conditions

$$u(0) = 0, \quad v(0) = 0, \quad u(1) = -U_y(1)h, \quad v(1) = -i\omega h, \quad p(1) = Thk^2, \qquad (3.20)$$

which is expressed in streamfunction form as (3.6*a*) subject to

$$\phi(0) = 0, \quad kU_y(1)\phi(1) + \omega\phi_y(1) = 0, \qquad (3.21a)$$

$$\phi_y(0) = 0, \quad (ikR)^{-1}(\phi_{yyy}(1) - k^2\phi_y(1)) - U_y(1)^{-1}Tk^2\phi_y(1) = 0. \qquad (3.21b)$$

This is the undamped version of the local stability problem studied by Stewart *et al.* (2010*b*). Again the eigenvalues and eigenfunctions are generated using a Chebyshev

spectral method (Appendix A.1). The local eigenvalue spectrum now consists of four surface-based modes (two TWF and two SD) which we denote by $k_{s,j}$ ($j = 1, 2, 3, 4$; s for surface-based) and infinitely many hydrodynamic modes, which, for $j = 1, 2, \ldots$, we denote by k_j, ordered as in the rigid segment, as illustrated in figure 2(*b*). The corresponding eigenfunctions are, respectively, denoted by $q_{s,j}$ and q_j. The Womersley mode does not satisfy the boundary conditions in the compliant segment (3.21).

Thus, a flow in the compliant segment of the channel is expressed as a modal expansion in the form

$$q(x, y; \omega) = \sum_{j=1}^{\infty} c_j q_j(y) e^{ik_j x} + \sum_{j=1}^{4} c_{s,j} q_{s,j}(y) e^{ik_{s,j} x} \quad (0 < x < L), \qquad (3.22)$$

where the constants c_j and $c_{s,j}$ are unknown and can be complex.

We now proceed to match the expansions from the rigid (see (3.19)) and compliant (see (3.22)) segments together, before applying suitable global boundary conditions.

3.1.3. *Matching between compartments*

To make the problem numerically tractable, we truncate each of the infinite sums in (3.19*a*, *b*) and (3.22) to M hydrodynamic modes.

Matching between compartments is straightforward when hydrodynamic modes are ignored, as the surface-based modes in the compliant segment and the Womersley mode in the rigid segments cannot propagate across the junctions. Jensen & Heil (2003), implicitly using this truncation in the high-frequency limit, matched fluxes and pressures between compartments to predict an asymptotic stability threshold for $T \gg 1$ (illustrated in figure 3*a*).

However, the hydrodynamic modes propagate in all three compartments of the channel, and upon reaching a junction a given mode is scattered into all the other modes in both compartments either side of the junction. We capture this behaviour following Manuilovich (2004). Continuity of q across the junction at $x = 0$ implies that

$$c_{u,0} q_{u,0} + \sum_{j=1}^{M} c_{u,j} q_{u,j} = \sum_{j=1}^{M} c_j q_j + \sum_{j=1}^{4} c_{s,j} q_{s,j} \quad (x = 0). \qquad (3.23a)$$

We pre-multiply both sides of (3.23*a*) by H (see (3.16)) and take the inner product (3.7) with the set of eigenfunctions adjoint to the rigid modes, $\{q_0^\dagger, q_1^\dagger, \ldots, q_M^\dagger\}$. By exploiting the orthogonality condition (3.15), (3.23*a*) can be rearranged to give

$$c_u = R c + R' c_s, \qquad (3.23b)$$

where R and R' are matrices representing the scattering of the modes in the upstream rigid segment into the hydrodynamic and surface-based modes in the compliant segment, respectively, and $c_u = (c_{u,0}, c_{u,1}, \ldots, c_{u,M})$, $c = (c_1, c_2, \ldots, c_M)$ and $c_s = (c_{s,1}, c_{s,2}, c_{s,3}, c_{s,4})$ are vectors of unknown coefficients. The matrices R and R' are

$$R_{nm} = \frac{\langle q_n^\dagger, H q_m \rangle}{\langle q_n^\dagger, H q_{u,m} \rangle} \quad (m = 1, \ldots, M; n = 0, \ldots, M), \qquad (3.23c)$$

$$R'_{nm} = \frac{\langle q_n^\dagger, H q_{s,m} \rangle}{\langle q_n^\dagger, H q_{u,m} \rangle} \quad (m = 1, \ldots, 4; n = 0, \ldots, M). \qquad (3.23d)$$

Similarly, continuity of $\boldsymbol{q}$ across the junction at $x = L$ implies that

$$c_{d,0}\boldsymbol{q}_{d,0} + \sum_{j=1}^{M} c_{d,j}\boldsymbol{q}_{d,j}\mathrm{e}^{\mathrm{i}k_{r,j}L} = \sum_{j=1}^{M} c_j\boldsymbol{q}_j\mathrm{e}^{\mathrm{i}k_jL} + \sum_{j=1}^{4} c_{s,j}\boldsymbol{q}_{s,j}\mathrm{e}^{\mathrm{i}k_jL} \quad (x = L). \qquad (3.24a)$$

This can be expressed in the form

$$\boldsymbol{D}\boldsymbol{c}_d = \boldsymbol{S}\boldsymbol{E}\boldsymbol{c} + \boldsymbol{S}'\boldsymbol{F}\boldsymbol{c}_s, \qquad (3.24b)$$

where $\boldsymbol{S}$ and $\boldsymbol{S}'$ are scattering matrices and $\boldsymbol{c}_d = (c_{d,0}, c_{d,1}, \ldots, c_{d,M})$ is a vector of unknown coefficients. $\boldsymbol{D}$, $\boldsymbol{E}$ and $\boldsymbol{F}$ are diagonal matrices such that

$$D_{00} = 1, \quad D_{mm} = \mathrm{e}^{\mathrm{i}k_{r,m}L} \quad (m = 1, \ldots, M), \qquad (3.24c)$$

$$E_{mm} = \mathrm{e}^{\mathrm{i}k_m L} \quad (m = 1, \ldots, M), \qquad (3.24d)$$

$$F_{mm} = \mathrm{e}^{\mathrm{i}k_{s,m}L} \quad (m = 1, \ldots, 4). \qquad (3.24e)$$

The matrices $\boldsymbol{S}$ and $\boldsymbol{S}'$ take the form

$$S_{nm} = \frac{\langle \boldsymbol{q}_n^\dagger, \boldsymbol{H}\boldsymbol{q}_m \rangle}{\langle \boldsymbol{q}_n^\dagger, \boldsymbol{H}\boldsymbol{q}_{d,m} \rangle} \quad (m = 1, \ldots, M; n = 0, \ldots, M), \qquad (3.24f)$$

$$S'_{nm} = \frac{\langle \boldsymbol{q}_n^\dagger, \boldsymbol{H}\boldsymbol{q}_{s,m} \rangle}{\langle \boldsymbol{q}_n^\dagger, \boldsymbol{H}\boldsymbol{q}_{d,m} \rangle} \quad (m = 1, \ldots, 4; n = 0, \ldots, M). \qquad (3.24g)$$

3.1.4. *Global boundary conditions*

We require the perturbation height of the flexible membrane to be zero at the upstream and downstream ends of the compliant segment ($x = 0, x = L$), which implies that

$$\sum_{j=1}^{M} c_j h_j + \sum_{j=1}^{4} c_{s,j} h_{s,j} = 0 \quad (x = 0), \qquad (3.25a)$$

$$\sum_{j=1}^{M} c_j h_j \mathrm{e}^{\mathrm{i}k_j L} + \sum_{j=1}^{4} c_{s,j} h_{s,j} \mathrm{e}^{\mathrm{i}k_{s,j}L} = 0 \quad (x = L). \qquad (3.25b)$$

Strictly, we also require the perturbation pressure to be zero at the extreme upstream and downstream ends of the channel ($x = -L_1$, $x = L + L_2$), assuming that each rigid segment is long enough for the flow to be unidirectional at the channel's inlet and outlet. Rather than enforce this exactly, we approximate this condition in the upstream (downstream) rigid segment by suppressing all modes which are exponentially growing upstream (downstream) by setting their coefficients $c_{u,j}$ ($c_{d,j}$) to zero. This results in exponentially small pressure fluctuations at the channel ends, but prevents wave reflections at the channel ends from contributing to the generation of global instabilities. This is a modelling assumption that we test against simulations below.

To close, the system requires one more condition at each junction. Following Manuilovich (2004), we match the pressure pointwise at $(0, 1)$ and $(L, 1)$, so that

$$c_{u,0} + \sum_{j=1}^{M} c_{u,j} p_{u,j}(1) = \sum_{j=1}^{M} c_j p_j(1) + \sum_{j=1}^{4} c_{s,j} p_{s,j}(1) \quad (x = 0), \qquad (3.26a)$$

$$c_{d,0} + \sum_{j=1}^{M} c_{d,j} p_{d,j}(1)\mathrm{e}^{\mathrm{i}k_{r,j}L} = \sum_{j=1}^{M} c_j p_j(1)\mathrm{e}^{\mathrm{i}k_j L} + \sum_{j=1}^{4} c_{s,j} p_{s,j}(1)\mathrm{e}^{\mathrm{i}k_{s,j}L} \quad (x = L). \qquad (3.26b)$$

For fixed M, these conditions are distinct from the integral matching of perturbation pressure across the junctions in (3.23) and (3.24).

We therefore have a system of $2M + 6$ equations (see (3.23a), (3.24a), (3.25) and (3.26)) with $2M + 6$ unknowns ($c_u \in \mathbb{C}^{K+1}$, $c_d \in \mathbb{C}^{M-K+1}$, $c \in \mathbb{C}^M$ and $c_s \in \mathbb{C}^4$, assuming that we retain K exponentially decaying upstream modes and $M - K$ exponentially decaying downstream modes in the rigid segments). The system can be expressed in the form $Mb = 0$, where M is a known matrix and b is a vector of all the unknown coefficients. Neutrally stable global modes are computed by searching for curves in parameter space with real frequency where $\det(M) = 0$. To calculate a neutrally stable solution we fix the dimensionless membrane tension T and isolate the corresponding critical Reynolds number $R = R_c^{(M)}$ and frequency $\omega = \omega_c^{(M)}$ (where $\text{Re}(\det(M)) = \text{Im}(\det(M)) = 0$). Details of the procedures used are given in Appendix A.2.

While this method of matched eigenfunction expansions provides insights into the manner in which hydrodynamic modes contribute to global instability, it has certain limitations as a numerical approximation. The imposition of both pointwise (see (3.26)) and integral pressure-matching conditions, and the non-normality of the spatial operators, can be expected to lead to ill-conditioning. Indeed, we find that for large M, the determinant of the matrix M becomes close to zero for all values of the parameters ω and R; some hydrodynamic modes have almost identical eigenvalues and eigenfunctions; so M loses rank. However, we obtain useful results for M between 0 and 7 that we compare against full simulations in §4.

3.2. *Computational method*

We also performed direct numerical simulations of the fully coupled fluid–structure interaction problem with oomph-lib. For this purpose, we discretized the arbitrary Lagrangian–Eulerian form of the two-dimensional unsteady Navier–Stokes equations (2.1) with quadrilateral Taylor–Hood (Q2Q1) elements. One-dimensional Hermite elements were used to discretize the equations governing the deformation of a pre-stressed thin-walled massless Kirchhoff–Love beam. We set the wall thickness to $\hbar/\mathfrak{a} = 1/100$ to ensure that bending effects remained small and subjected the ends of the beam to 'pinned' boundary conditions, fixing their positions but allowing them to rotate freely. Time derivatives were discretized with a second-order backwards difference (BDF2) scheme with the time step chosen so that each period contained approximately 160 steps. The fluid mesh contained a larger number of elements near the walls to ensure that the Stokes layers were fully resolved. Typical production runs were performed with discretizations that involved approximately 16 000 degrees of freedom. Selected computations were repeated with a doubled temporal and spatial resolution to assess the mesh and time-step independence of the results.

Simulations were performed in a two-stage procedure. First, writing the external pressure distribution (2.5) as $p_e(x) = P(x) + p_\delta$, for given parameters (R and T), we used a displacement-control technique to compute the value of p_δ required to deform the elastic wall such that its midpoint was deflected outwards by 0.1 % of the channel width. This slightly inflated steady configuration was then used as the initial condition for a time-dependent simulation during which oscillations were initiated by setting $p_\delta = 0$ for $t \geqslant 0$. Following the decay of initial transients, the wall performed growing or decaying small-amplitude oscillations about the undeformed configuration. We determined the period and growth/decay rates of these oscillations by a Levenberg–Marquardt fit to an exponentially growing/decaying harmonic oscillation. The critical Reynolds number $R_c(T)$ at which the system undergoes a Hopf bifurcation to a mode 1 oscillation was determined by interpolation. We assessed the criticality of the Hopf

bifurcation by performing simulations with different initial amplitudes. The critical Reynolds number was not affected by the amplitude of the initial deflection, indicating that the bifurcation is supercritical, at least for the parameter values investigated.

3.3. *Energy*

As $\mathcal{K}$ in (2.9) is an exact time derivative and $\mathscr{E}$ can be written as

$$\mathscr{E} = \int_0^L h_t(p_e - Th_{xx})\,\mathrm{d}x = \frac{\mathrm{d}}{\mathrm{d}t}\left(\int_0^L \left(hp_e + \frac{1}{2}Th_x^2\right)\mathrm{d}x\right), \tag{3.27}$$

the time average over the period of an oscillation (denoted with an overbar) of the full energy budget (2.9*a*) can be expressed as

$$0 = \overline{\mathscr{P}} + \overline{\mathscr{F}} - \overline{\mathscr{D}}. \tag{3.28}$$

Expanding using (3.1) to $O(\theta^2)$, (2.8) can be expressed as a leading-order Reynolds–Orr equation entirely in terms of $O(\theta)$ variables (see Appendix B):

$$\tfrac{1}{2}\left(u_1^2 + v_1^2\right)_t + \tfrac{1}{2}U\left(3u_1^2 + v_1^2\right)_x + (u_1 p_1)_x + (v_1 p_1)_y$$
$$- R^{-1}(u_1\nabla^2 u_1 + v_1\nabla^2 v_1) + U(-u_1 u_{1,x} - v_1 u_{1,y}) = 0. \tag{3.29}$$

The corresponding perturbation energy budget can then be expressed in terms of products of first-order variables (with energy components denoted with hats) as

$$\hat{\mathscr{K}} + \hat{\mathscr{E}} = \hat{\mathscr{P}} + \hat{\mathscr{F}} - \hat{\mathscr{D}} - \hat{\mathscr{S}}, \tag{3.30a}$$

where

$$\hat{\mathscr{K}} = \frac{\mathrm{d}}{\mathrm{d}t}\left(\int_{-L_1}^{L+L_2}\int_0^1 \frac{1}{2}\left(u_1^2 + v_1^2\right)\mathrm{d}y\,\mathrm{d}x\right), \tag{3.30b}$$

$$\hat{\mathscr{E}} = \int_0^L (v_1 p_1)\Big|_{y=1}\,\mathrm{d}x, \tag{3.30c}$$

$$\hat{\mathscr{P}} = -\left[\int_0^1 u_1 p_1\,\mathrm{d}y\right]_{x=-L_1}^{x=L+L_2}, \tag{3.30d}$$

$$\hat{\mathscr{F}} = -\left[\int_0^1 \frac{1}{2}U\left(3u_1^2 + v_1^2\right)\mathrm{d}y\right]_{x=-L_1}^{x=L+L_2}, \tag{3.30e}$$

$$\hat{\mathscr{D}} = -R^{-1}\int_{-L_1}^{L+L_2}\int_0^1 (u_1\nabla^2 u_1 + v_1\nabla^2 v_1)\,\mathrm{d}y\,\mathrm{d}x, \tag{3.30f}$$

$$\hat{\mathscr{S}} = -\int_{-L_1}^{L+L_2}\int_0^1 U(u_1 u_{1,x} + v_1 u_{1,y})\,\mathrm{d}y\,\mathrm{d}x. \tag{3.30g}$$

$\hat{\mathscr{S}}$ is the rate of energy production by nonlinear Reynolds stresses. As in (3.27), $\hat{\mathscr{E}}$ can be expressed as a complete time derivative. Taking the perturbation pressure of the global mode to be zero at the extreme upstream and downstream ends of the channel implies that $\hat{\mathscr{P}} = 0$. Integrating by parts, $\hat{\mathscr{D}}$ can be written as

$$\hat{\mathscr{D}} = R^{-1}\int_{-L_1}^{L+L_2}\int_0^1 \left\{\left(u_{1,x}^2 + u_{1,y}^2 + v_{1,x}^2 + v_{1,y}^2\right) - (u_1 u_{1,x} + v_1 v_{1,x})_x\right\}\mathrm{d}y\,\mathrm{d}x$$

$$- R^{-1}\int_0^1 \left[u_1 u_{1,y} + v_1 v_{1,y}\right]^{y=1}\,\mathrm{d}x. \tag{3.31}$$

Thus, if $u_{1,x} = v_1 = 0$ at the entrance and exit of the channel, the exact x-derivative in (3.31) can be eliminated, leaving a positive-definite term and one of indeterminate signs (e.g. Domaradzki & Metcalfe 1987; Guaus & Bottaro 2007), showing how viscous effects at the membrane can be destabilizing. Taking the time average of (3.30), we obtain

$$0 = \overline{\hat{\mathcal{F}}} - \overline{\hat{\mathcal{D}}} - \overline{\hat{\mathcal{S}}}. \tag{3.32}$$

This relationship provides a useful independent check of the accuracy of predictions from modal expansions, while also giving insights into the underlying physical mechanisms.

Alternatively, we can express (2.9a) to $O(\theta^2)$ (see Appendix B), writing the energy budget so that it includes second-order variables (with energy components denoted with breves) as

$$\hat{\mathcal{K}} + \check{\mathcal{K}} + \hat{\mathcal{E}} + \check{\mathcal{E}} = \hat{\mathcal{P}} + \check{\mathcal{P}} + \hat{\mathcal{F}} + \check{\mathcal{F}} - \hat{\mathcal{D}} - \check{\mathcal{D}}, \tag{3.33}$$

where

$$\check{\mathcal{K}} = \frac{\mathrm{d}}{\mathrm{d}t}\left(\int_{-L_1}^{L+L_2}\int_0^1 U u_2 \,\mathrm{d}y\,\mathrm{d}x\right), \tag{3.34a}$$

$$\check{\mathcal{E}} = \int_0^L (v_2 P)\Big|_{y=1}\,\mathrm{d}x, \tag{3.34b}$$

$$\check{\mathcal{P}} = -\left[\int_0^1 (U p_2 + P u_2)\,\mathrm{d}y\right]_{x=-L_1}^{x=L+L_2}, \tag{3.34c}$$

$$\check{\mathcal{F}} = -\left[\int_0^1 \frac{3}{2}U^2 u_2 \,\mathrm{d}y\right]_{x=-L_1}^{x=L+L_2}, \tag{3.34d}$$

$$\check{\mathcal{D}} = -R^{-1}\int_{-L_1}^{L+L_2}\int_0^1 (U\nabla^2 u_2 + U_{yy}u_2)\,\mathrm{d}y\,\mathrm{d}x. \tag{3.34e}$$

From (3.30) and (3.33), it follows that

$$\check{\mathcal{K}} + \check{\mathcal{E}} = \check{\mathcal{P}} + \check{\mathcal{F}} - \check{\mathcal{D}} + \hat{\mathcal{S}}, \tag{3.35}$$

which has the time average

$$0 = \overline{\check{\mathcal{P}}} + \overline{\check{\mathcal{F}}} - \overline{\check{\mathcal{D}}} + \overline{\hat{\mathcal{S}}}. \tag{3.36}$$

We see how time-averaged Reynolds stresses exchange energy between oscillations (3.32) and steady adjustments to the mean flow (3.36). We can also take the time average of (3.35) directly to recover the complete energy budget (3.28) truncated to $O(\theta^2)$:

$$0 = \overline{\check{\mathcal{P}}} + \left(\overline{\hat{\mathcal{F}}} + \overline{\check{\mathcal{F}}}\right) - \left(\overline{\check{\mathcal{D}}} + \overline{\hat{\mathcal{D}}}\right). \tag{3.37}$$

Jensen & Heil (2003) showed that for neutrally stable sloshing oscillations with $L_1 < L_2$, (3.37) is partitioned according to

$$\overline{\hat{\mathcal{D}}} \approx \tfrac{2}{3}\overline{\hat{\mathcal{F}}}, \quad \overline{\check{\mathcal{D}}} - \overline{\check{\mathcal{P}}} \approx \overline{\hat{\mathcal{S}}} \approx \tfrac{1}{3}\overline{\hat{\mathcal{F}}}, \quad \overline{\check{\mathcal{F}}} \ll 1 \quad \text{as } T \to \infty, \tag{3.38}$$

implying that two-thirds of the energy extracted from the mean flow (due to an asymmetry in kinetic energy fluxes at either end of the compliant segment of channel) is dissipated by oscillatory sloshing motion, the remaining third being balanced by adjustments to the mean flow.
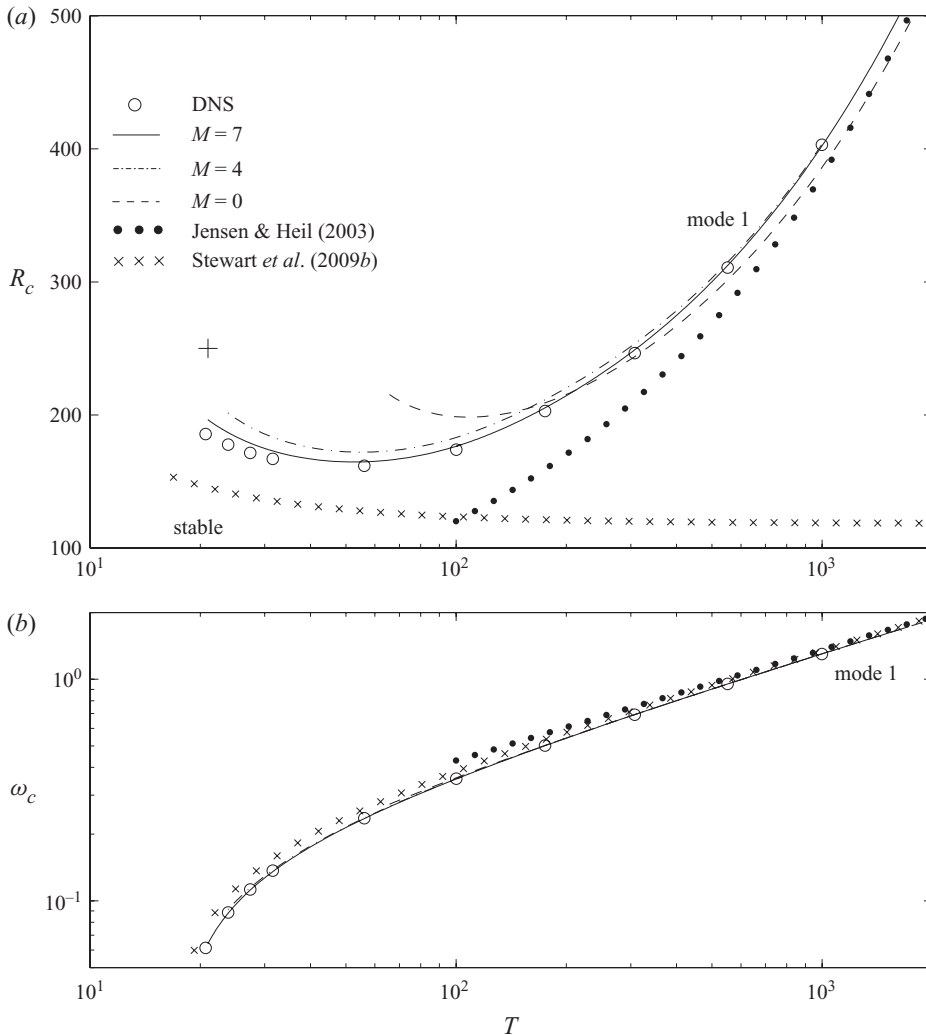
FIGURE 3. (*a*) Neutral stability curve for the primary global instability showing estimates of critical Reynolds number R_c versus membrane tension T; (*b*) corresponding frequencies versus T. Predictions using eigenfunction expansions are shown using truncations $M = 7$ (solid line), $M = 4$ (dot-dashed line) and $M = 0$ (dashed line). Filled black circles correspond to predictions of Jensen & Heil (2003) given in (4.1) and open circles correspond to two-dimensional direct numerical simulations (DNS). Small crosses show the prediction of the one-dimensional model (see (2.11)), from Stewart *et al.* (2009). Nonlinear oscillations at the point identified by + in (*a*) are illustrated in figures 7 and 8.

4. Small-amplitude mode 1 oscillations

4.1. *The mode 1 neutral curve*

Of the five governing parameters given in (2.2), we fix $L = 10$, $L_1 = 5$ and $L_2 = 30$ (as in Jensen & Heil 2003) and focus our attention on the neutral curve $R = R_c(T)$ in (R, T) parameter space across which the uniform state loses stability to mode 1 oscillations through a Hopf bifurcation. For the parameter regimes investigated in the two-dimensional simulations, the bifurcation was always supercritical, with mode 1 becoming unstable for $R > R_c$. Values of R_c and the associated frequencies ω_c obtained

M	T	$R_c^{(M)}$	% error	$\omega_c^{(M)}$	T	$R_c^{(M)}$	% error	$\omega_c^{(M)}$
0	1000	386.2	4.2	1.3016	100	198.7	14.3	0.3590
1	1000	dnc	dnc	dnc	100	199.7	14.8	0.3602
2	1000	405.3	0.54	1.3027	100	210.7	21.2	0.3606
3	1000	405.3	0.54	1.3027	100	210.8	21.2	0.3606
4	1000	403.8	0.17	1.3025	100	183.1	5.2	0.3557
5	1000	402.8	0.07	1.3024	100	187.6	7.9	0.3563
6	1000	402.4	0.16	1.3024	100	182.7	5.0	0.3562
7	1000	402.4	0.16	1.3024	100	176.5	1.5	0.3547

TABLE 1. Predictions of critical Reynolds number $R_c^{(M)}$ and frequency $\omega_c^{(M)}$ for a modal truncation involving M hydrodynamic modes, computed using $N = 50$ Chebyshev polynomials. The calculation labelled 'dnc' did not converge satisfactorily. The percentage error refers to the relative error between R_c (determined from two-dimensional simulations) and R_c^M.

from two-dimensional simulations are shown with circles in figure 3, providing a benchmark for testing alternative approximations. The frequency of neutral mode 1 oscillations falls from high values at large T towards zero near $T = 20$ (figure 3*b*).

We first assess the convergence properties of the method of matched eigenfunctions truncated at M hydrodynamic modes (§ 3.1), yielding predictions denoted by $R_c^{(M)}$ and $\omega_c^{(M)}$. Table 1 illustrates the improvement in predictions achieved by increasing M at $T = 1000$ and $T = 100$, showing the relative error in R_c compared to two-dimensional simulations. The error is greater for smaller T, but is still under 2 % for $T = 100$ with $M = 7$. The improvement in error with M is gradual and not always monotonic.

To further assess the accuracy of the modal expansions, the spatial structure of neutrally stable self-excited oscillations at $T = 1000$ and $T = 100$ for $M = 7$ is illustrated in figure 4, which shows instantaneous streamlines of the perturbation flow field at five time points over a half-period of oscillation; the background colour map and near-vertical contours indicate the perturbation pressure. The remaining half of the oscillation period can be inferred by symmetry. All quantities have been normalized to ensure that the maximal height of the membrane is 0.05 at its midpoint. In both cases shown, the streamlines vary smoothly across the junctions. Both examples are typical sloshing oscillations, with transverse deflection of the membrane coupled to axial flows in the rigid segments. Axial sloshing is more vigorous in the upstream rigid segment, where there is lower total fluid inertia. Whenever the wall comes to rest, fluid inertia drives instantaneous recirculation in the compliant segment of the channel ($0 < x < L$) (figure 4*a*, *e*, *f*, *j*); this vortex is notably absent over much of the remainder of the oscillation. Small cross-stream pressure gradients are evident in the compliant segment of the channel.

Returning to figure 3(*a*), we now compare $R_c^{(0)}(T)$, $R_c^{(4)}(T)$ and $R_c^{(7)}(T)$ with predictions of R_c from two-dimensional simulations. At fixed tension, there is convergence towards the predictions from simulations as M increases. It was possible to extend predictions of R_c to lower values of T for larger values of M, but, for each truncation, it was not possible to track the neutral curves to the point at which $\omega_c \to 0$. However, with $M = 7$, the turning point in the neutral curve near $T = 55$ is predicted well (for the points presented, the relative error between R_c and $R_c^{(7)}$ is at most 6.3 %), whereas this feature is not caught by $R_c^{(0)}$, demonstrating the importance of hydrodynamic modes in this region of parameter space. Conversely, hydrodynamic modes are not needed to obtain good estimates of frequencies (figure 3*b*).
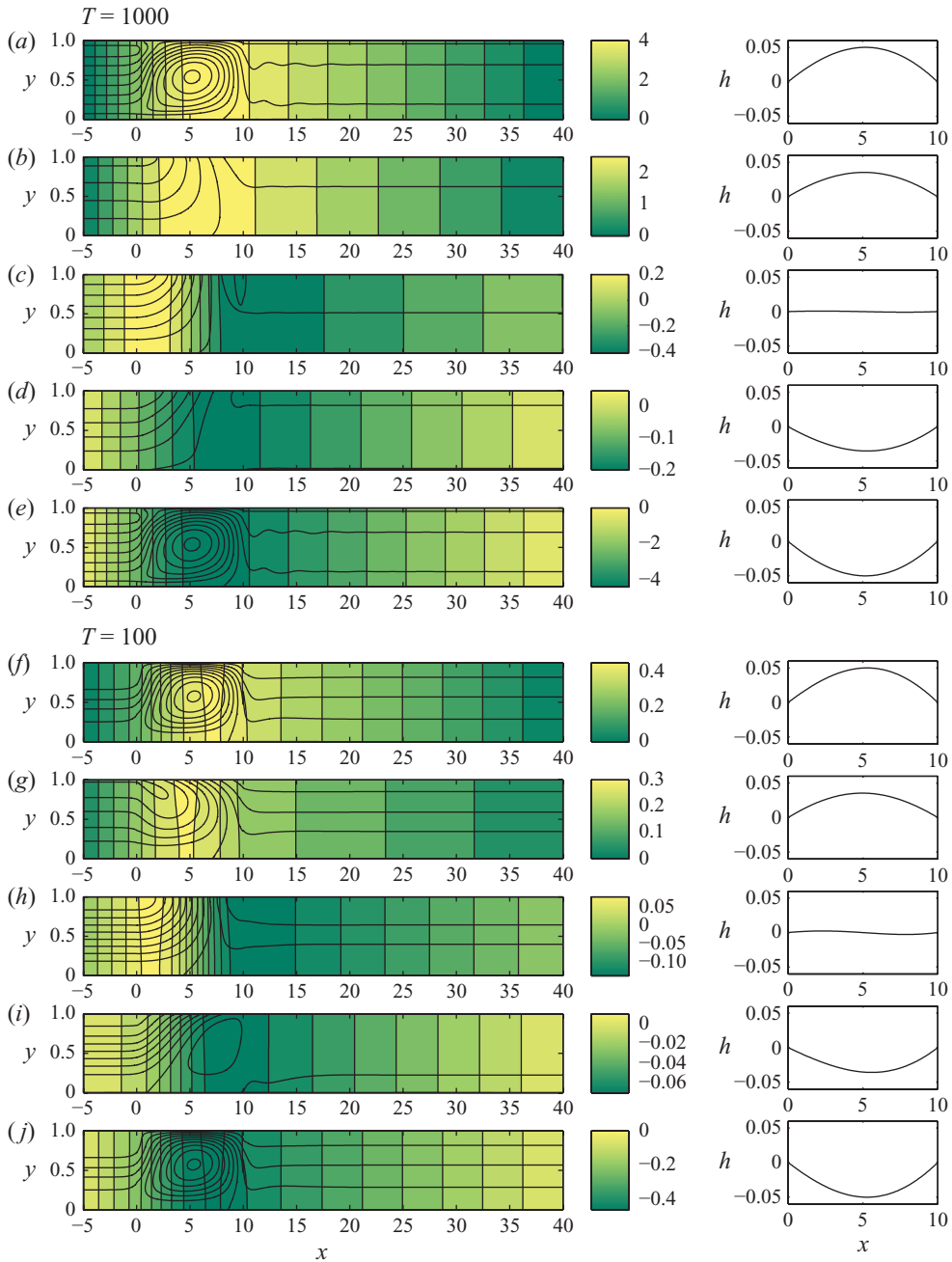
FIGURE 4. (Colour online) Left-hand panels show instantaneous perturbation streamlines of the flow over half a period of oscillation generated using $M = 7$ for $(a–e)$ $T = 1000$ and $(f–j)$ $T = 100$; the shading shows the pressure perturbation in the channel, over a scale indicated by the colour map to the right of each subfigure. The corresponding wall shape is shown to the right of each panel.

For comparison, we also show in figure 3 the asymptotic prediction of R_c and ω_c in the limit $T \gg 1$ due to Jensen & Heil (2003), given by

$$R_c \approx r_{c0}^2 T^{1/2}, \quad \omega_c \approx \beta T^{1/2}/L^2, \tag{4.1}$$

where the constants r_{c0} and β depend on the lengths of the channel segments. (The parameter r_{c0} falls as L_2 increases and increases rapidly as $L_2 - L_1 > 0$ decreases to zero; here we do not attempt to further survey the effect of varying L_1 or L_2.) In the present example, $r_{c0} \approx 3.469$ and $\beta \approx 4.2915$. This approximation is effectively an $M = 0$ truncation involving long-wavelength, high-frequency approximations of the SD and TWF modes in the compliant segment of the channel, and of the Womersley mode in the rigid segments; continuity of pressure and flux are imposed across the internal junctions. Thus, it differs marginally at large T from the $M = 0$ truncation used to determine $R_c^{(0)}$, which involves eigensolutions of the Orr–Sommerfeld equation computed at finite wavenumber. Even at $T = 1000$, both predictions differ slightly from two-dimensional simulations because of the neglect of hydrodynamic modes, but nevertheless both capture the dominant behaviour well.

It is also instructive to test the predictions of the simplified one-dimensional model of the same system (2.11), in which viscous and convective inertial effects are crudely represented by averaging an assumed parabolic velocity profile. For $T \gg 1$, high-frequency sloshing oscillations are predicted by the one-dimensional model (Stewart *et al.* 2009), which captures ω_c accurately (this being determined by a simple balance between membrane tension and fluid inertia, see figure 3*b*). Inevitably, however, the prediction of R_c is inaccurate for large T (figure 3*a*) as the one-dimensional model cannot estimate the appropriate scaling for viscous dissipation in Stokes layers. Nevertheless, at lower tensions the one-dimensional model is in surprisingly good qualitative agreement with R_c and ω_c obtained by two-dimensional simulations. This is significant, as it lends weight to predictions of the one-dimensional model in nearby regions of parameter space. In particular, the one-dimensional model predicts that the neutral curve terminates at a co-dimension 2 point near $T = 20$ (Stewart *et al.* 2009), at which the mode 1 frequency vanishes, suggesting the likelihood of a nearby homoclinic bifurcation. The one-dimensional model also exhibits nonlinear 'slamming' oscillations close to the mode 1 neutral curve (see figure 9), which we examine in more detail in § 5.

4.2. *Excitation of eigenmodes*

Traces in the k-plane of the hydrodynamic and surface-based eigenvalues contributing to mode 1 neutral oscillations as T is decreased are shown in figure 5(*a*). Significantly, the downstream-propagating TWF mode becomes spatially unstable as the tension decreases ($\text{Im}(k) = 0$, $\text{Re}(k) = 0.1541$ at $T \approx 152.0$, $R_c^{(7)} \approx 196.7$, $\omega_c^{(7)} \approx 0.461$; figure 5*a*, inset), suggesting that local instability can contribute to the global response. Furthermore, as the frequency of the global mode approaches zero, the wavenumber of this TWF mode approaches the origin in the k-plane (figure 5*a*, inset), a feature also captured in the one-dimensional model (Stewart *et al.* 2009). As the membrane tension decreases, the wavenumbers of three of the hydrodynamic modes ('1(u)', '2(d)' and '7(d)') approach values marked with crosses in figure 5(*a*) lying at

$$k = -\beta \mathrm{i}, \quad k = -\beta\left(\pm\sin\frac{6\pi}{7} + \mathrm{i}\cos\frac{6\pi}{7}\right), \quad \beta \equiv \frac{(180|\mathrm{Ai}'(0)|)^{3/7}}{(6R)^{1/7}}. \qquad (4.2)$$

This triad of quasi-static modes (with $\omega \to 0$) is captured by interactive boundary-layer theory for a flow in a rigid channel (see figure 3 of Bogdanova & Ryzhov 1983, from where (4.2) is derived); these modes also appear as poles of the Fourier transform used by Guneratne & Pedley (2006) in their study of static instabilities in the two-dimensional Starling resistor analogue. The remaining hydrodynamic modes move towards the positive half of the imaginary axis in the k-plane as T decreases.

In figure 5(*b–d*), we trace the amplitudes of each of the local eigenfunctions that constitute the global mode for decreasing membrane tension (with $M = 7$).
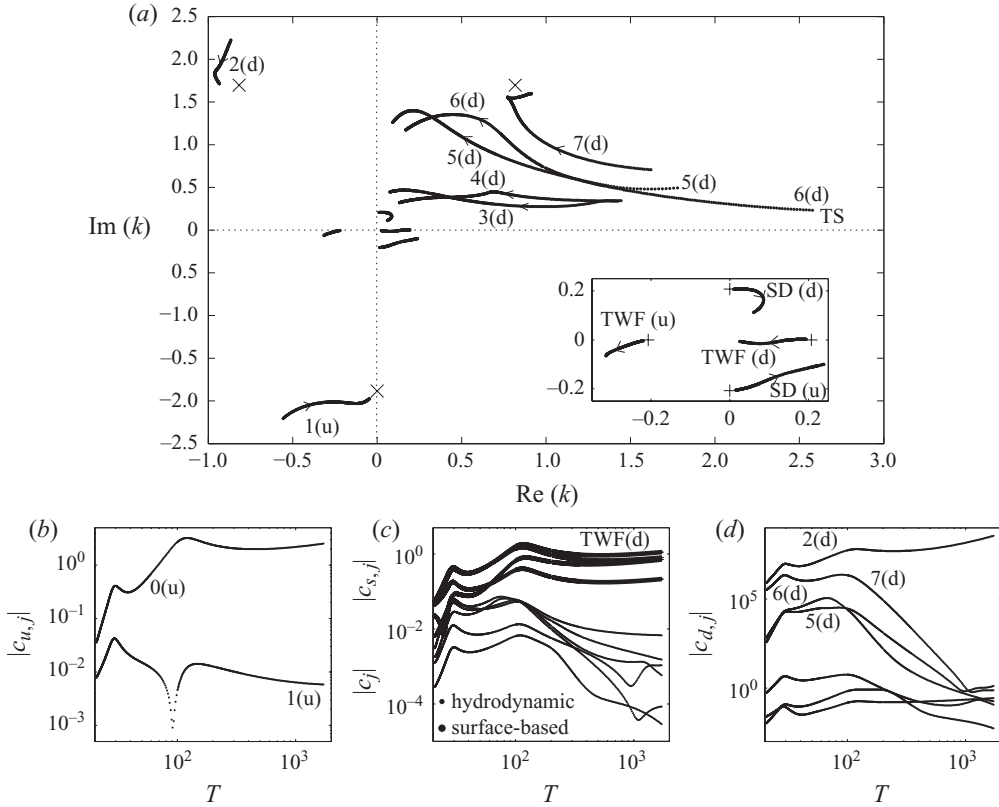
FIGURE 5. (*a*) Traces of the hydrodynamic (1–7) and wall (SD and TWF) modes in the wavenumber plane as tension is decreased along the neutral curve for $M = 7$ in figure 3. The arrows indicate the direction of decreasing tension. Crosses indicate the limiting solutions (4.2) plotted for $R = 200$. The symbols in the inset represent the asymptotic prediction of the surface-based modes from Jensen & Heil (2003). (*b*–*d*) Relative amplitudes of each of the local modes for tension decreasing along the neutral curve for $M = 7$ in figure 3: (*b*) in the upstream rigid segment; (*c*) in the compliant segment (the mode labelled '1' is not shown as its amplitude is much less than all the others); (*d*) in the downstream rigid segment. At $T = 1000$, modes are ordered by decreasing amplitude as TWF(d), TWF(u), SD(d), SD(u), 2, 6, 3, 5, 4, 7, 1 in (*c*), and 2, 7, 5, 6, 0, 3, 4 in (*d*). Labels correspond to those used in (*a*) and in figure 2.

In this figure, the local eigenmodes are re-normalized to have unit kinetic energy such that $(\int_0^h (|u|^2 + |v|^2)\, dy)/2 = 1$ (although similar results are obtained under the normalization given in Appendix A.1). The Womersley mode is dominant in the upstream rigid segment, and the four surface-based modes are dominant in the compliant segment. The greatest contribution in the downstream rigid segment for all T comes from the most rapidly decaying (in x) hydrodynamic mode labelled '2' in figure 2, although this mode is not needed to predict R_c when $T \gg 1$ (Jensen & Heil 2003). As the membrane tension is decreased, other hydrodynamic modes (particularly those labelled '5–7') become relatively important; however, the TS mode ('6') remains stable at these low Reynolds numbers.

4.3. *Energy budget for mode 1 oscillations*

Jensen & Heil (2003) identified a mechanism for sloshing oscillations at $T \gg 1$ in terms of energy transfer, showing a remarkably simple 2:1 partition of kinetic energy
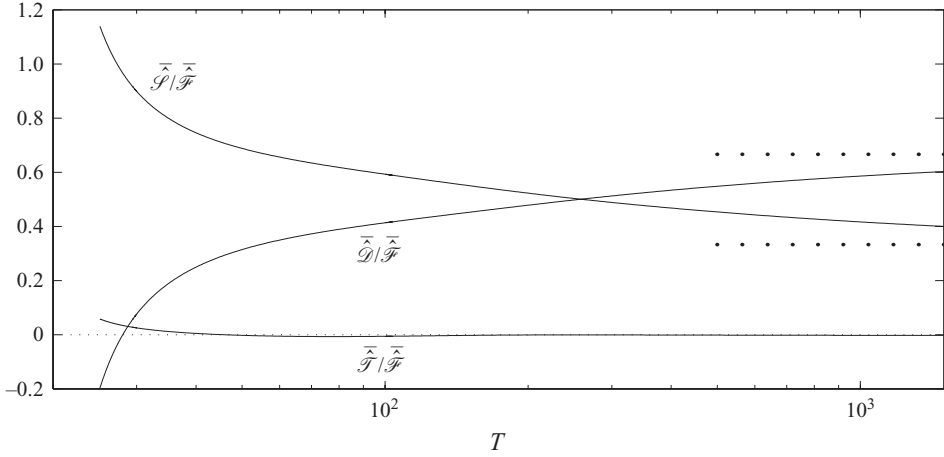
FIGURE 6. Ratio of terms in the time-averaged energy budget (3.32) as a function of membrane tension T using $M = 7$, showing the relative truncation error, $\overline{\hat{\mathcal{T}}}/\overline{\hat{\mathcal{F}}}$, the relative perturbation to the rate of viscous dissipation, $\overline{\hat{\mathcal{D}}}/\overline{\hat{\mathcal{F}}}$, and the relative perturbation rate of working of Reynolds stresses $\overline{\hat{\mathcal{S}}}/\overline{\hat{\mathcal{F}}}$. Dots indicate the asymptote (3.38).

fluxes (see (3.38)). We now seek to understand how energy budgets change at lower tensions with hydrodynamic modes included.

The time-averaged perturbation energy budget (3.32) provides a useful method for estimating the error in the modal approximation, arising through a combination of truncation errors in the spectral method, matching errors across junctions and in the application of the global boundary conditions. We denote this error by

$$\overline{\hat{\mathcal{T}}} = \overline{\hat{\mathcal{F}}} - \overline{\hat{\mathcal{D}}} - \overline{\hat{\mathcal{S}}}, \tag{4.3}$$

where $\overline{\hat{\mathcal{F}}}$, $\overline{\hat{\mathcal{D}}}$ and $\overline{\hat{\mathcal{S}}}$ are computed from truncated modal expansions. As we can expect slight discontinuities across the junctions between rigid and compliant segments, we evaluate $\hat{\mathcal{F}}$ using the sum

$$\hat{\mathcal{F}} = -\left[\int_0^1 \frac{1}{2} U \left(3u_1^2 + v_1^2 \right) \mathrm{d}y \right]_{x=-L_1}^{x=0}$$
$$-\left[\int_0^1 \frac{1}{2} U \left(3u_1^2 + v_1^2 \right) \mathrm{d}y \right]_{x=0}^{x=L} - \left[\int_0^1 \frac{1}{2} U \left(3u_1^2 + v_1^2 \right) \mathrm{d}y \right]_{x=L}^{x=L+L_2}. \tag{4.4}$$

Computations indicate that $\overline{\hat{\mathcal{F}}}$ remains positive along the mode 1 neutral curve, although it falls monotonically towards zero as T decreases. We therefore illustrate the relative error in our approximation by plotting $\overline{\hat{\mathcal{T}}}/\overline{\hat{\mathcal{F}}}$ for decreasing T (figure 6). The relative error remains low in the limit $T \to \infty$, but gradually increases as hydrodynamic modes become more important at low tensions. For example with $M = 7$, the relative error at $T = 25.0$ is 5.9 %.

The normalized perturbation rate of dissipation, $\overline{\hat{\mathcal{D}}}/\overline{\hat{\mathcal{F}}}$, and Reynolds stress, $\overline{\hat{\mathcal{S}}}/\overline{\hat{\mathcal{F}}}$, are also plotted versus T in figure 6. The ratio $\overline{\hat{\mathcal{D}}}/\overline{\hat{\mathcal{F}}}$ slowly approaches 2/3 for $T \gg 1$, which is consistent with (3.38). For sufficiently low tensions, however, $\overline{\hat{\mathcal{D}}}$ becomes negative ($\overline{\hat{\mathcal{D}}} = 0$ for $T \approx 28$ for $M = 7$), by an amount substantially larger
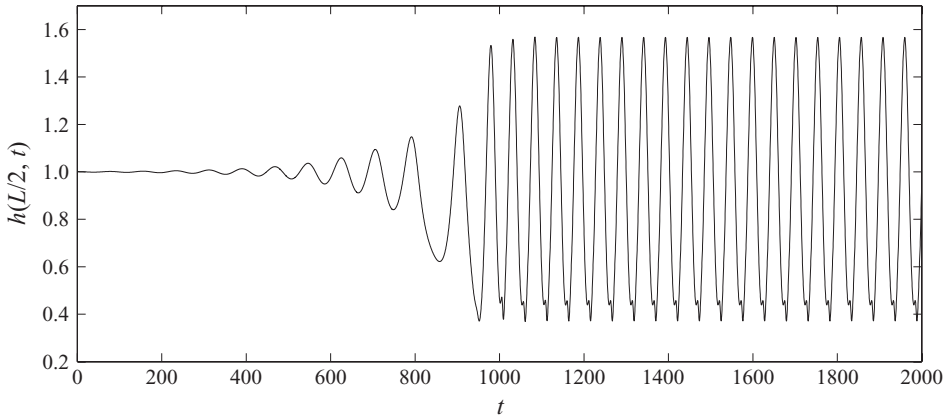
FIGURE 7. Evolution of the membrane midpoint $h(L/2, t)$, from two-dimensional simulations, showing a linearly unstable mode 1 oscillation saturating to a large-amplitude limit cycle exhibiting periodic 'slamming', for $T = 21$, $R = 250$, $L_1 = 5$, $L_2 = 30$ and $L = 10$.

than the error $\overline{\hat{T}}$, implying that oscillatory viscous effects in the flexible channel segment act as an energy source (see (3.31)), and suggesting a fundamental change in the mechanism of oscillations compared to that identified by Jensen & Heil (2003). We conjecture that this is linked to the downstream TWF mode, which is destabilized through the action of a weak critical layer at the channel centreline (figure 5a; Stewart *et al.* 2010b). In contrast, the energy exchanged between time-averaged oscillations and the mean flow by nonlinear Reynolds stresses, $\overline{\hat{\mathscr{S}}}$, slowly approaches $\overline{\hat{\mathscr{F}}}/3$ for $T \gg 1$ (consistent with (3.38)), but increases (relative to $\overline{\hat{\mathscr{F}}}$) as T falls.

   We also computed each of the terms in (2.9) by two-dimensional simulation, in order to estimate the balance of terms in the time-averaged total energy budget (3.28). For a given T, we considered a simulation with $R \approx R_c$ and computed $\mathscr{F}(t)$, $\mathscr{P}(t)$ and $\mathscr{D}(t)$. Extracting a meaningful time average was difficult as the oscillation was either slowly growing or decaying in time. For each quantity of interest, we therefore fitted the growth of the maximal and minimal points of the oscillation separately; using these growth rates, we then extrapolated the maximal and minimal points to approximate the mid-line of the oscillation. We found, for example, that at $T = 1000$, $\overline{\mathscr{F}} \approx 8.3 \times 10^{-5}$, whereas at $T = 31.6$, $\overline{\mathscr{F}} \approx 3.09 \times 10^{-6}$ (for the same amplitude). While these results suggest that the time-averaged kinetic energy flux $\overline{\mathscr{F}}$ decreases with decreasing membrane tension, we did not see evidence of a change of sign in $\overline{\mathscr{F}}$.

5. Large-amplitude oscillations: 'slamming' motion

   We now consider finite-amplitude oscillations that arise beyond the mode 1 neutral curve. An example was given by Jensen & Heil (2003) for $T = 100$ and $R = 450$, showing how vigorous sloshing motion excites secondary instabilities within the channel. We highlight here a robust feature of oscillations at lower tensions, namely a low-frequency periodic 'slamming' motion, which we now describe briefly using both two-dimensional simulations (§ 5.1) and by constructing a simplified analytical model (§ 5.2).

5.1. *Nonlinear simulations*

Figure 7 shows the time evolution (from two-dimensional simulation) of the midpoint of the membrane at $R = 250$, $T = 21$ (illustrated with a cross in figure 3a), a point beyond the threshold for instability to mode 1 oscillations. The mode 1
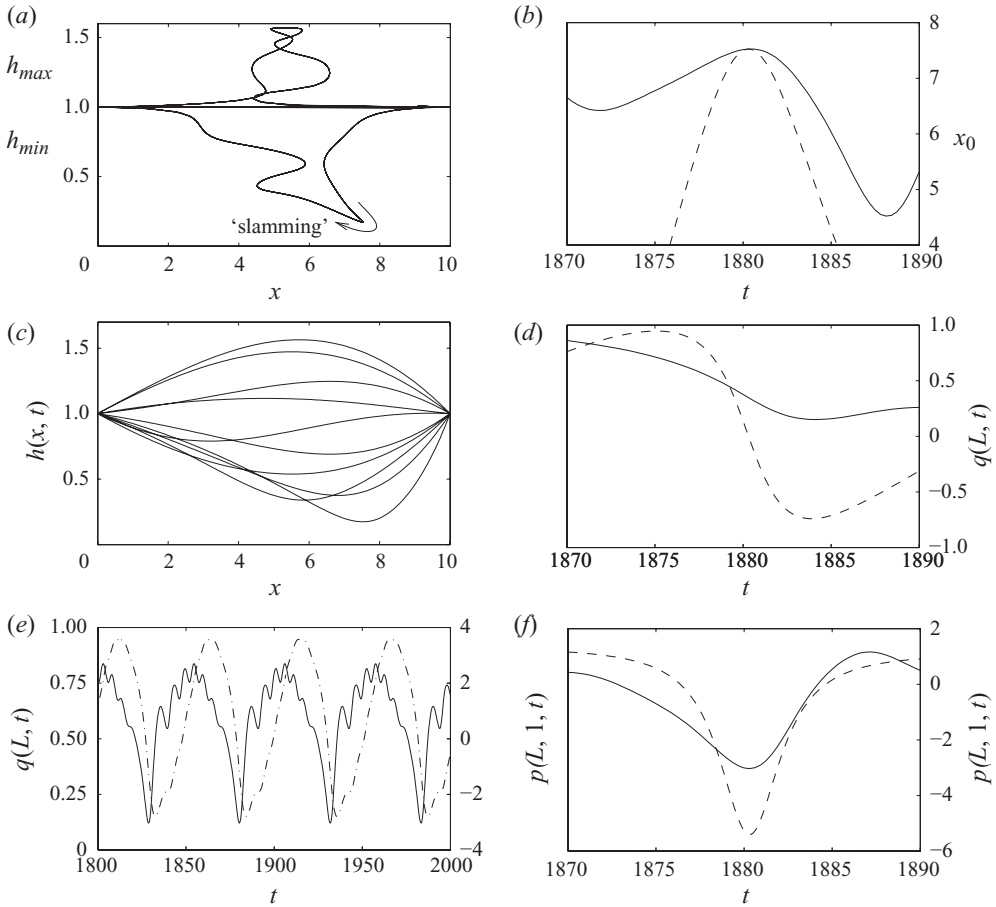
FIGURE 8. 'Slamming' motion predicted using two-dimensional simulations at $T = 21$ and $R = 250$ (as in figure 7). Left column: (a) a phase portrait showing the maximum and minimum heights of the membrane against their corresponding spatial positions; (c) 10 membrane profiles over a period; (e) pressure $p(L, 1, t)$ (solid) and flux $q(L, t)$ (dot-dashed) at the downstream end of the compliant segment. Right column: comparison between two-dimensional simulation (solid lines) and the reduced model (5.6) (dashed lines) around the interval of greatest collapse; (b) time trace of the position of the membrane minimum, $x_{min}(t) \equiv x_0(t)$; (d) downstream flux $q(L, t)$; (f) downstream pressure $p(L, 1, t)$.

oscillation grows rapidly before saturating as a large-amplitude periodic limit cycle, shown in figure 8 and the animation in the supplementary material. In figure 8(a), the coordinates of local extrema of membrane displacement $(x_{min}(t), h_{min}(t))$ and $(x_{max}(t), h_{max}(t))$ are traced out. As is evident from figure 8(a) and the solid curve in figure 8(b), the membrane moves close to the rigid wall at a point near the downstream end of the compliant segment, before quickly recovering, an event we describe as 'slamming'. Simultaneously, the flux at the downstream end of the compliant segment, $q(L, t)$, falls close to zero and the local pressure, $p(L, 1, t)$, falls to low values over a short interval (see figure 8e and the solid curves in figure 8d, f). Slamming appears to trigger a damped oscillation in the pressure trace (six local post-slam maxima are evident in $p(L, 1, t)$, separated by a minimum time interval of approximately 1/10th of a period); the accompanying animation (see supplementary material) shows the dynamics of the full flow and pressure field in more detail.
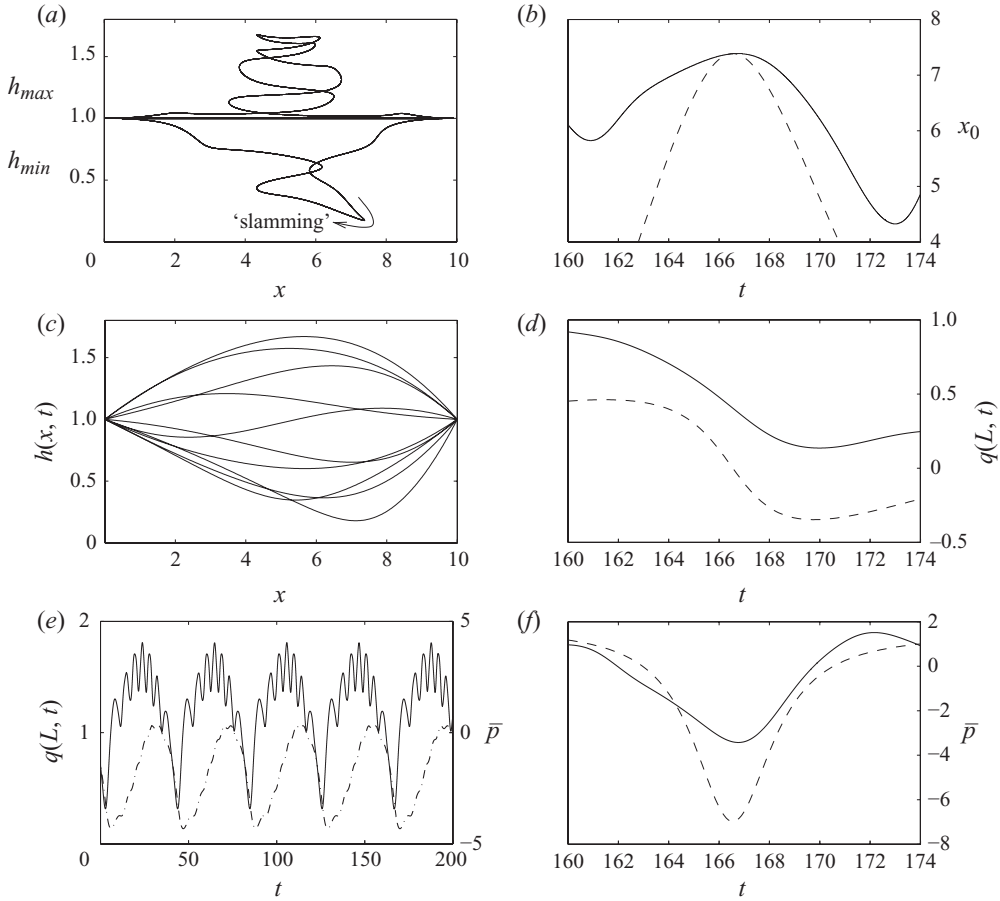
FIGURE 9. 'Slamming' motion predicted using the one-dimensional model (2.11) at $T = 30$, $R = 200$. Left column: (a) a phase portrait showing the maximum and minimum heights of the membrane against their corresponding spatial positions; (c) 10 membrane profiles over a period; (e) cross-sectionally averaged pressure $\bar{p} = L_2(q_t + 12q/R)$ (solid line) and flux $q(L, t)$ (dot-dashed line) at the downstream end of the compliant segment. Right column: comparison between the solutions of the one-dimensional model (2.11) (solid lines) and the reduced model (5.6) (dashed lines) around the interval of greatest collapse; (b) location of constriction $x_0(t)$; (d) flux $q(L, t)$ versus t; (f) $\bar{p}$ versus t.

Similar behaviour is evident in solutions of the one-dimensional model (2.11), solved using the numerical scheme described in Stewart *et al.* (2009) and shown in figure 9 for $R = 200$ and $T = 30$. (As the one-dimensional model is based on an *ad hoc* closure approximation, we cannot expect quantitative agreement with two-dimensional simulations, and indeed R_c is underpredicted by around 20 % at $T = 30$ in figure 3. Furthermore, nonlinear oscillations significantly beyond the neutral curve in the one-dimensional model exhibit secondary bifurcations such as period doubling that are sensitive to parameter choices. We therefore did not attempt to exactly match parameters with figure 8, but have instead selected two representative examples illustrating some common features.) The phase portraits and flux and pressure traces in figure 9(a, c), and in the solid curves in figure 9(b, d, f), clearly resemble figure 8, particularly in the brief slamming phase. In this instance, the pressure trace exhibits seven distinct local post-slam minima, again separated by minimum time interval

of approximately 1/10th of a period. For other parameters, even more vigorous slamming was observed. It is natural to ask what drives this near-singular behaviour.

5.2. *Reduced model for 'slamming' behaviour*

To understand the physical processes underlying a slamming event, we now build a 'toy' model that seeks to characterize as simply as possible its dominant qualitative features. This approach is inspired by previous 'lumped-parameter' models of the Starling resistor (Bertram & Pedley 1982; Armitstead, Bertram & Jensen 1996), although these did not represent the effects of axial tension or axial motion of the constriction.

We approximate the pressure in the compliant segment of the channel using (2.7). Let the minimum height of the membrane in the compliant segment be $h_0(t) \equiv h_{min}(t)$, with corresponding spatial position $x_0(t) \equiv x_{min}(t)$, so that $h_x(x_0, t) = 0$. In the short region between this minimum and the junction with the downstream rigid segment ($x_0 < x < L$), the external pressure is uniform to leading order, $p_e \approx P_e \equiv 12L_2 R^{-1}$. We assume that the internal fluid pressure $p = p_0(t)$ is also approximately uniform in this region, so that $Th_{xx} \approx P_e - p_0$ in $x_0 < x < L$ (linearizing the membrane curvature for simplicity). When the channel is almost constricted ($0 < h_0 \ll 1$), we impose the approximate boundary conditions $h = h_x = 0$ at $x = x_0$ and $h = 1$ at $x = L$, implying that

$$h = \frac{(x - x_0)^2}{(L - x_0)^2}, \quad x_0 = L - \left(\frac{2T}{P_e - p_0} \right)^{1/2} \quad (x_0 < x < L). \quad (5.1)$$

To determine the corresponding volume flux $q(x, t)$, we use (5.1) and (2.11a); integrating across $x_0 < x < L$ yields

$$q = q_0 + \frac{1}{3} x_{0,t} \frac{(x - x_0)^2}{(L - x_0)^3} (3L - 2x - x_0) \quad (x_0 < x < L), \quad (5.2)$$

where $q_0(t) \equiv q(x_0, t)$ is the flux through the constriction. It follows that the flux at the downstream end of the compliant segment, and hence throughout the downstream rigid segment, is controlled by axial displacement of the constriction: $q(L, t) = q_0 + (x_{0,t}/3)$. We assume for simplicity that, during the most vigorous phase of slamming motion, q_0 can be neglected relative to $x_{0,t}$.

The corresponding pressure drop along the downstream rigid segment has viscous and inertial contributions that we estimate following the approach used to derive (2.11), recognizing the limitations of this approach in accurately capturing the dissipation of rapidly accelerating flows. Assuming for simplicity that the flow in the downstream segment is a uniform Poiseuille flow, $u = 6qy(1 - y)$, the x-momentum equation, when integrated across the channel, reduces to

$$q_t = -p_x - 12R^{-1}q \quad (L < x < L + L_2), \quad (5.3)$$

from which we calculate $p_0 = L_2(q_t + 12R^{-1}q)$, giving, with (5.1b), two expressions for the pressure and an evolution equation for $x_0(t)$:

$$p_0 = P_e - \frac{2T}{(L - x_0)^2} = \frac{L_2}{3} \left[\frac{12}{R} x_{0,t} + x_{0,tt} \right]. \quad (5.4)$$

We now use (5.4) to model one cycle of slamming motion. We let L_0 be the minimum separation between $x = x_0$ and $x = L$, assumed to occur at $t = t_0$, so that $x_{0,t}(t_0) = 0$ and $x_0(t_0) = L - L_0$, and then rescale using

$$x_0 = L - L_0 \check{L}(\check{t}), \quad t = t_0 + \left(L_0^3 L_2/(6T) \right)^{1/2} \check{t}, \quad (5.5)$$

so that (5.4) reduces to a two-parameter problem defined by

$$\check{L}_{\check{t}\check{t}} = \frac{1}{\check{L}^2} - \left(\frac{24 L_2 L_0^3}{R^2 T}\right)^{1/2} \check{L}_{\check{t}} - \frac{P_e L_0^2}{2T}, \quad \check{L}(0) = 1, \quad \check{L}_{\check{t}}(0) = 0. \tag{5.6}$$

The corresponding physical variables are

$$q(L, t) = -\left(\frac{2T}{3 L_0 L_2}\right)^{1/2} \check{L}_{\check{t}}, \quad p(L, 1, t) = P_e - \frac{2T}{(L_0 \check{L})^2}. \tag{5.7}$$

Solutions of (5.6), segments of a damped nonlinear oscillation, are plotted as dashed curves alongside data from two-dimensional simulations in figure 8(b, d, f), and one-dimensional predictions in figure 9(b, d, f), having fitted only L_0 and t_0. Given the crude approximations made in deriving (5.6), we do not expect a precise quantitative match with simulations. Nevertheless, there is reasonable qualitative agreement between predictions of the reduced model and simulations around the point of greatest collapse. Viscous effects, which are small for the parameter values chosen, lead to a slight asymmetry between the advancing and receding motion of the constriction. The term involving the external pressure P_e in (5.6) causes the oscillation to saturate. The approximate model could be refined to include the flux q_0 (which is not determined locally), which would modify the degree of saturation and would also account for the fact that the flow does not undergo complete reversal. However, even without q_0, the simple reduced model provides a useful physical interpretation of the slamming motion. Downstream movement of the constriction increases the curvature of the membrane in $x_0 < x < L$, and is accompanied by a fall in pressure to negative values, leading to an adverse pressure gradient in the downstream rigid segment, decelerating the column of fluid downstream of the constriction; fluid is then driven back into the compliant segment of the channel from the downstream end, pushing the constriction upstream. Mass conservation implies that the constriction must move upstream, which results in a decrease in the membrane curvature and an increase in the fluid pressure.

Neglecting the relatively weak effects of dissipation in the downstream segment and external pressure in (5.6a), we can interpret the system as a nonlinear spring, with fluid inertia in the downstream segment balancing the elastic restoring force due to membrane curvature, the two effects determining the time scale of the slamming event via (5.5b). Lubrication effects are likely to have a role to play in inhibiting opposite-wall contact at the constriction: when $x_{0,t} > 0$ and $h(x_0, t) \ll 1$, $h(x_0, t)$ may be determined by the speed of advance of the constriction through the Landau–Levich–Bretherton mechanism familiar from thin-film coating problems (Landau & Levich 1942; Bretherton 1961).

6. Discussion

We have used two complementary approaches to investigate the stability of a uniform Poiseuille flow in the two-dimensional Starling resistor analogue (figure 1), namely a method of matched eigenfunction expansions and two-dimensional computational simulation. We restricted attention to the primary oscillatory instability that arises when the pressure is specified at both ends of the system, namely mode 1 oscillations involving a single-humped disturbance to the membrane location (examples of which are illustrated in figure 4). By evaluating predictions of the mode 1 neutral curve from truncated eigenfunction expansions against two-dimensional simulations (figure 3), we have demonstrated how small-amplitude mode 1 oscillations

change character as the membrane tension T is reduced. The mechanism of instability at high T has been explained previously both at the local level (being driven by wave reflections of SD and TWF modes at the junctions with the rigid channel segments; Stewart *et al.* 2009) and at the global level (the shorter upstream rigid channel segment enabling sloshing flows to extract energy from the mean flow via asymmetric kinetic energy fluxes; Jensen & Heil 2003). Both levels of description must be modified to understand mode 1 oscillations at lower T. First, the downstream-propagating TWF component of a mode 1 oscillation can grow spatially (figure 5*a*, inset), showing how a local instability mechanism may contribute to global instability through viscous effects operating at a weak critical layer at the channel centreline (Stewart *et al.* 2010*b*). Second, and consistent with observations of the global energy budget, $\widehat{\overline{\mathcal{D}}}$ (the time-averaged perturbation to the rate of dissipation due to oscillatory motion) becomes negative as T falls (figure 6), implying that viscous effects are destabilizing through a reduction in dissipation rate. Meanwhile, Reynolds stresses, which transfer energy from the oscillations to the mean flow, increase relatively (figure 6). The local viscous mechanism that destabilizes TWF is potentially responsible for the global reduction in dissipation rate as T falls: however, a simple mechanistic explanation is hampered by the intricate spatial distribution of sources and sinks revealed by Stewart *et al.* (2010*b*), through which energy is exchanged between perturbation dissipation and Reynolds stresses (two of the three components in (3.32)).

It is evident from figure 3(*a*) that hydrodynamic modes contribute to mode 1 oscillations at lower tensions, although the dominant eigenmodes in the downstream rigid segment are those labelled 2 and 7 (figure 5*d*), visible as decaying waves in streamline plots (e.g. figure 4*a*, *f*), rather than mode 6, the TS mode. In the parameter regime considered here, we saw no evidence of the dramatic excitation of vorticity waves reported in other computational studies (Luo & Pedley 1996; Luo *et al.* 2008), which considered configurations with non-uniform base states, and in experiments in channels with moving constrictions (Stephanoff *et al.* 1983; Pedley & Stephanoff 1985). We have conjectured elsewhere that transient growth effects may be responsible for the excitation and spatial localization of vorticity waves in collapsible channel oscillations (Stewart *et al.* 2010*a*). The associated non-normality of the spatial linear operator in (3.6) and (3.21) is also likely to limit the accuracy of the present eigenfunction-expansion method, motivating the future use of a complete global stability analysis (as initiated by Luo *et al.* 2008). Such an analysis would also be useful in assessing the importance of pressure reflections from the extreme ends of the channel, a feature neglected from the present modal analysis.

We are not aware of experiments that might allow us to test our predictions of the two-dimensional Starling resistor analogue directly. While a sloshing instability has been predicted to operate in three dimensions theoretically (the present eigenfunction-expansion approach has been adopted with effectively an $M = 0$ truncation in the long-wave, high-frequency limit by Whittaker *et al.* 2010*b*), experiments in the appropriate parameter regime, either in a channel or a tube, are still awaited. There are, however, previous reports that we can relate to 'slamming' behaviour (figures 8 and 9). This is characterized by periodic rapid drops in pressure at the downstream end of the compliant segment (commonly denoted by p_2 in experiments), followed by a quick recovery; there is a corresponding abrupt fall of flux (denoted by q_2) with a slower recovery. Similar behaviour has been reported, for example in simulations, using alternative one-dimensional models (Bertram, Sheppeard & Jensen 1994; Hayashi, Hayase & Kwamura 1998). In experiments, nonlinear oscillations sharing features with slamming have been reported as 'LU' oscillations (Bertram *et al.* 1990) and

'type C' oscillations (Xia *et al.* 2000). However, these experiments reveal features not seen in our simulations: for example, over the parameter regime investigated, we did not observe 'sucking' behaviour in which the elastic segment is drawn into the downstream rigid segment, as occurs when the axial pre-stress is sufficiently small (Xia *et al.* 2000). Our simple analytical model (§ 5.2), describing only the brief time interval around the spike, does not make predictions about the dynamics of the overall oscillation, but instead seeks to explain the mechanism by which a balance of elastic and inertial effects provide the restoring force that drives the pressure and flux recovery. In particular, the model predicts that the time scale of the slamming event increases with the inertia of fluid in the downstream rigid segment (the time scale being proportional to $L_s^{1/2}$ in (5.5)). This is consistent with data reported in figure 8 of Wang, Chew & Low (2009), who showed a clear increase in the recovery time of p_2 and q_2 with increased downstream inertance. There are many features of the simplified model that might be refined usefully in future studies, including using fully nonlinear membrane curvature, representation of viscous dissipation in Stokes layers and proper allowance for axial wall motion.

In summary, we have shown, using a combination of complementary approaches, how hydrodynamic modes can play an important role in determining the onset of mode 1 oscillations in collapsible channel flows, and how local viscous effects may contribute to the growth of a global instability. We have also shown how both small-amplitude sloshing and large-amplitude slamming oscillations involve an inviscid interaction between elastic-wall deformations and fluid inertia, particularly that in the rigid segments of the channel. It will be of interest to see to what extent these ideas are relevant to more complex wall models (including dissipation and inertia) and fully three-dimensional effects, when additional effects such as mode interactions (Mandre & Mahadevan 2010) and symmetry-breaking bifurcations (Heil & Boyle 2010) come into play.

Supplementary data are available at journals.cambridge.org/flm.

Appendix A. Numerical method
A.1. *Spectral method for local eigenmodes*

To implement the modal analysis described in § 3.1, we require the solution of the local stability problem in both the rigid (see (3.6)) and compliant (see (3.21)) segments of the channel, as well as the adjoint problem in the rigid segments (3.11). We use a Chebyshev spectral method (Schmid & Henningson 2001; Peyret 2002) similar to that described and used previously by Stewart *et al.* (2010*b*). In summary, the flow domain ($0 \leqslant y \leqslant 1$) is rescaled to the numerical domain ($-1 \leqslant Y \leqslant 1$) using the transformation $Y = 2y - 1$, $\Phi(Y) = \phi(y)$ and the streamfunction is expanded as a series of N Chebyshev polynomials in the form

$$\Phi = \sum_{n=0}^{N} a_n Z_n(Y), \qquad (A\,1)$$

where Z_n is the nth Chebyshev polynomial and a_n are unknown numerical coefficients. To implement the problem numerically, we use collocation at the Gauss–Lobatto points $Y_j = \cos(j\pi/N)$ for $j = 0, \ldots, N$ (Peyret 2002).

We consider disturbances of fixed real frequency ω, at a given R and T, and examine eigenvalue spectra in the wavenumber plane, employing the companion matrix method (Bridges & Morris 1984) to solve the nonlinear eigenvalue problem. As the corresponding eigenfunctions are inaccurate close to the boundaries, we use the eigenvalues generated using the companion matrix method as an initial estimate and employ Newton iteration to identify roots of the corresponding temporal stability problem (where the wavenumber is fixed and we consider eigenvalue spectra in the frequency) with complex wavenumber k that have the desired real frequency ω. Since the Reynolds numbers of the global modes under consideration are typically less than $R = 500$, we found that 50 Chebyshev polynomials were sufficient to resolve the eigenvalue spectra to the required accuracy. For each of the surface-based and hydrodynamic modes (as well as their adjoints in the rigid segments), the vector of spectral coefficients $a_1, a_2, \ldots, a_n$ was normalized to ensure a 2-norm of one. The Womersley modes were calculated analytically using (3.15) and expressed at the Gauss–Lobatto collocation points; these modes were normalized to have a pressure of unity at the upstream and downstream junctions with the compliant segments, so that

$$\bar{A} = 1/L_1, \quad \bar{B} = L_1 \quad (-L_1 < x < 0), \tag{A 2a}$$

$$\bar{A} = -1/L_2, \quad \bar{B} = -L - L_2 \quad (L < x < L + L_2). \tag{A 2b}$$

A.2. *Construction of global modes*

To compute global modes, we construct the matrix $\boldsymbol{M}$ using the normalized eigenfunctions computed by MATLAB and compute the determinant numerically. To calculate a neutrally stable solution, we fix the dimensionless membrane tension T and use the function `fminsearch` in MATLAB to isolate the corresponding critical Reynolds number $R_c^{(M)}$ and frequency $\omega_c^{(M)}$ (where abs(det($\boldsymbol{M}$)) = 0) using a relative error tolerance of 10^{-4}. However, the system loses sensitivity as M increases (the determinant of the matrix tends to zero for all values of the parameters T, R and ω) and isolating the zeros of the real and imaginary parts of det($\boldsymbol{M}$) becomes computationally more expensive. For $M = 7$, it was necessary to multiply the eigenfunction by a normalization constant which increases the determinant of the matrix without altering the zeros.

Appendix B. Energetics of neutrally stable modes

To capture the energy budget of neutrally stable oscillations using the modal analysis of §3.1, we look at $O(\theta^2)$ disturbances in (2.1), governed by

$$u_{2,x} + v_{2,y} = 0, \tag{B 1a}$$

$$u_{2,t} + U u_{2,x} + U_y v_2 + p_{2,x} - R^{-1}(u_{2,xx} + u_{2,yy}) = -u_1 u_{1,x} - v_1 u_{1,y}, \tag{B 1b}$$

$$v_{2,t} + U v_{2,y} + p_{2,y} - R^{-1}(v_{2,xx} + v_{2,yy}) = -u_1 v_{1,x} - v_1 v_{1,y}, \tag{B 1c}$$

subject to

$$u_2 = 0, \quad v_2 = 0 \quad (y = 0,\ -L_1 < x < L + L_2), \qquad (B\,1d)$$

$$u_2 = 6h_2 + 6h_1^2 - u_{1,y}h_1, \quad v_2 = h_{2,t} \quad (y = 1,\ 0 < x < L), \qquad (B\,1e)$$

$$u_2 = 0, \quad v_2 = 0 \quad (y = 1,\ -L_1 < x < 0,\ L < x < L + L_2). \qquad (B\,1f)$$

A normal stress balance determines the shape of the compliant membrane

$$p_2 = -Th_{2,xx} \quad (y = 1,\ 0 < x < L). \qquad (B\,1g)$$

Nonlinear Reynolds stresses on the right-hand side of (B 1b, c) force u_2, v_2 and p_2; in particular, if u_1, v_1 and p_1 are periodic, then u_2, v_2 and p_2 will have steady components, resulting in a 'weak' $O(\theta^2)$ change to the mean flow. The corresponding energy equation (2.8) in the compliant segment of the channel ($0 < x < L$) reduces with error $O(\theta^2)$ to

$$\tfrac{1}{2}\left(u_1^2 + v_1^2\right)_t \mathrm{d}y + \tfrac{1}{2}U\left(3u_1^2 + v_1^2\right)_x + (u_1 p_1)_x + (v_1 p_1)_y - R^{-1}(u_1 \nabla^2 u_1 + v_1 \nabla^2 v_1)$$

$$+ Uu_{2,t} + U^2 u_{2,x} + UU_y v_2 + Up_{2,x} + (u_2 P)_x - R^{-1}(U\nabla^2 u_2 + U_{yy}u_2) = 0, \quad (B\,2)$$

or equivalently, using (B 1), to the leading-order Reynolds–Orr equation (3.29). The energy equation in the rigid portion of the channel is identical, but no work is done across the rigid wall at $y = 1$ due to the no-penetration condition. Integrating (B 2), each term in the energy budget has a term arising from the product of two first-order variables (denoted with a hat) and a term arising from a combination of the mean flow and a second-order variable (denoted with a breve). Thus, (2.9a) can be written as (3.33). Following arguments presented in Stewart *et al.* (2010b), noting how nonlinear Reynolds stresses appear in (3.29), we may alternatively express (2.9) to $O(\theta^2)$ independently of u_2, v_2 and p_2 as (3.30a).

REFERENCES

ARMITSTEAD, J. P., BERTRAM, C. D. & JENSEN, O. E. 1996 A study of the bifurcation behaviour of a model of flow through a collapsible tube. *Bull. Math. Biol.* **58**, 611–641.

BERTRAM, C. D. 2008 Flow-induced oscillation of collapsed tubes and airway structures. *Respir. Physiol. Neurobiol.* **163**, 256–265.

BERTRAM, C. D. & PEDLEY, T. J. 1982 A mathematical model of unsteady collapsible tube behaviour. *J. Biomech.* **15**, 39–50.

BERTRAM, C. D., RAYMOND, C. D. & PEDLEY, T. J. 1990 Mapping of instabilities for flow through collapsed tubes of different length. *J. Fluids Struct.* **4**, 125–154.

BERTRAM, C. D., SHEPPEARD, M. D. & JENSEN, O. E. 1994 Prediction and measurement of area–distance profile of collapsed tubes during self-excited oscillation. *J. Fluids Struct.* **8**, 637–660.

BOGDANOVA, E. V. & RYZHOV, O. S. 1983 Free and induced oscillations in Poiseuille flow. *Q. J. Mech. Appl. Math.* **36**, 271–287.

BRETHERTON, F. P. 1961 The motion of long bubbles in tubes. *J. Fluid Mech.* **10**, 166–188.

BRIDGES, T. J. & MORRIS, P. J. 1984 Differential eigenvalue problems in which the parameter appears nonlinearly. *J. Comput. Phys.* **55**, 437–460.

CARPENTER, P. W. & GARRAD, A. D. 1985 The hydrodynamic stability of flow over Kramer-type compliant surfaces. Part 1. Tollmien–Schlichting instabilities. *J. Fluid Mech.* **155**, 465–510.

CARPENTER, P. W. & GARRAD, A. D. 1986 The hydrodynamic stability of flow over Kramer-type compliant surfaces. Part 2. Flow-induced surface instabilities. *J. Fluid Mech.* **170**, 199–232.

DAVIES, C. & CARPENTER, P. W. 1997 Instabilities in a plane channel flow between compliant walls. *J. Fluid Mech.* **352**, 205–243.

DEMPSEY, J. A., VEASEY, S. C., MORGAN, B. J. & O'DONNELL, C. P. 2010 Pathophysiology of sleep apnea. *Physiol. Rev.* **90**, 47–112.

DOMARADZKI, J. A. & METCALFE, R. W. 1987 Stabilization of laminar boundary layers by compliant membranes. *Phys. Fluids* **30**, 695–705.

ELEMANS, C. P. H., MULLER, M., NÆSBYE LARSEN, O. & VAN LEEUWEN, J. L. 2009 Amplitude and frequency modulation control of sound production in a mechanical model of the avian syrinx. *J. Exp. Biol.*, **212**, 1212–1224.

GROTBERG, J. B. & JENSEN, O. E. 2004 Biofluid mechanics in flexible tubes. *Annu. Rev. Fluid Mech.* **36**, 121–147.

GUAUS, A. & BOTTARO, A. 2007 Instabilities of the flow in a curved channel with compliant walls. *Proc. R. Soc. Lond.* A **463**, 2201–2222.

GUNERATNE, J. C. & PEDLEY, T. J. 2006 High-Reynolds-number steady flow in a collapsible channel. *J. Fluid Mech.* **569**, 151–184.

HAYASHI, S., HAYASE, T. & KWAMURA, H. 1998 Numerical analysis for stability and self-excited oscillation in collapsible tube flow. *Trans. ASME J. Biomech. Engng* **120**, 468–475.

HEIL, M. & BOYLE, J. 2010 Self-excited oscillations in three-dimensional collapsible tubes: onset and large amplitude oscillations. *J. Fluid Mech.* **652**, 405–426.

HEIL, M. & HAZEL, A. L. 2006 Oomph–lib: an object-oriented multi-physics finite-element library. In *Fluid–Structure Interaction* (ed. M. Schäfer & H.-J. Bungartz), pp. 19–49. Springer.

HEIL, M. & JENSEN, O. E. 2003 Flows in deformable tubes and channels. In *Flow in Collapsible Tubes and Past Other Highly Compliant Boundaries* (ed. P. W. Carpenter & T. J. Pedley). Kluwer.

HEIL, M. & WATERS, S. L. 2008 How rapidly oscillating collapsible tubes extract energy from a viscous mean flow. *J. Fluid Mech.* **601**, 199–227.

JENSEN, O. E. & HEIL, M. 2003 High-frequency self-excited oscillations in a collapsible-channel flow. *J. Fluid Mech.* **481**, 235–268.

KNOWLTON, F. P. & STARLING, E. H. 1912 The influence of variations in temperature and blood pressure on the performance of the isolated mammalian heart. *J. Physiol. Lond.* **44**, 206–219.

LANDAU, L. & LEVICH, B. 1942 Dragging of a liquid by a moving plate. *Acta Physicochim. URSS* **17**, 42–54.

LIU, H. F., LUO, X. Y., CAI, Z. X. & PEDLEY, T. J. 2009 Sensitivity of unsteady collapsible channel flows to modelling assumptions. *Commun. Numer. Meth. Engng* **25**, 483–504.

LUO, X. Y., CAI, Z. X., LI, W. G. & PEDLEY, T. J. 2008 The cascade structure of linear instability in collapsible channel flows. *J. Fluid Mech.* **600**, 45–76.

LUO, X. Y. & PEDLEY, T. J. 1996 A numerical simulation of unsteady flow in a two-dimensional collapsible channel. *J. Fluid Mech.* **314**, 191–225.

MANDRE, S. & MAHADEVAN, L. 2010 A generalized theory of viscous and inviscid flutter. *Proc. R. Soc. Lond.* A **466**, 141–156.

MANUILOVICH, S. V. 2004 Propagation of a Tollmien–Schlichting wave over the junction between rigid and compliant surfaces. *Fluid Dyn.* **39**, 702–717.

MILES, J. W. 1957 On the generation of surface waves by shear flows. *J. Fluid Mech.* **3**, 185–199.

PEDLEY, T. J. & LUO, X. Y. 1998 Modelling flow and oscillations in collapsible tubes. *Theor. Comput. Fluid Dyn.* **10**, 277–294 .

PEDLEY, T. J. & STEPHANOFF, K. D. 1985 Flow along a channel with a time-dependent indentation in one wall: the generation of vorticity waves. *J. Fluid Mech.* **160**, 337–367.

PEYRET, R. 2002 *Spectral Methods for Incompressible Viscous Flow*. Springer.

SCHMID, P. J. & HENNINGSON, D. S. 2001 *Stability and Transition in Shear Flows*. Springer.

SEN, P. K., CARPENTER, P. W., HEGDE, S. & DAVIES, C. 2009 A wave driver theory for vortical waves propagating across junctions with application to those between rigid and compliant walls. *J. Fluid Mech.* **625**, 1–46.

STEPHANOFF, K. D., PEDLEY, T. J., LAWRENCE, C. J. & SECOMB, T. W. 1983 Fluid flow along a channel with an asymmetric oscillating constriction. *Nature* **305**, 692–695.

STEWART, P. S., WATERS, S. L., BILLINGHAM, J. & JENSEN, O. E. 2010a Spatially localised growth within global instabilities of flexible channel flows. In *Seventh IUTAM Symposium on Laminar–Turbulent Transition* (ed. P. Schlatter & D. S. Henningson), vol. 18, pp. 397–402. Springer.

STEWART, P. S., WATERS, S. L. & JENSEN, O. E. 2009 Local and global instabilities of flow in a flexible-walled channel. *Eur. J. Mech.* B/*Fluids* **28**, 541–557.

STEWART, P. S., WATERS, S. L. & JENSEN, O. E. 2010b Local instabilities of flow in a flexible channel: asymmetric flutter driven by a weak critical layer. *Phys. Fluids* **22**, 031902.

THOMSON, S. L., MONGEAU, L. & FRANKEL, S. H. 2005 Aerodynamic transfer of energy to the vocal folds. *J. Acoust. Soc. Am.* **118**, 1689–1700.

WANG, J. W., CHEW, Y. T. & LOW, H. T. 2009 Effects of downstream system on self-excited oscillations in collapsible tubes. *Commun. Numer. Meth. Engng* **25**, 429–445.

WHITTAKER, R. J., HEIL, M., BOYLE, J. B., JENSEN, O. E. & WATERS, S. L. 2010a The energetics of flow through a rapidly oscillating tube. Part 2. Application to an elliptical tube. *J. Fluid Mech.* **648**, 123–153.

WHITTAKER, R. J., HEIL, M., JENSEN, O. E. & WATERS, S. L. 2010b The onset of high-frequency self-excited oscillations in elastic-walled tubes. *Proc. R. Soc. Lond.* A, doi:10.1098/rspa.2009.0641.

WHITTAKER, R. J., HEIL, M., JENSEN, O. E. & WATERS, S. L. 2010c A rational derivation of a tube law from shell theory. *Q. J. Mech. Appl. Maths*, doi:10.1093/qjmam/hbq020.

WHITTAKER, R. J., WATERS, S. L., JENSEN, O. E., BOYLE, J. B. & HEIL, M. 2010d The energetics of flow through a rapidly oscillating tube. Part 1. General theory. *J. Fluid Mech.* **648**, 83–121.

WOMERSLEY, J. R. 1955 Method for the calculation of velocity, rate of flow and viscous drag in arteries when the pressure gradient is known. *J. Physiol.* **127**, 553–563.

XIA, Y., HAYASE, T., HAYASHI, S. & HAMAYA, T. 2000 Effect of initial axial strain of collapsible tube on self-excited oscillation. *JSME Intl J. Ser. C Mech. Syst. Mach. Elem. Manuf.* **43**, 882–888.